SANDIA REPORT

SAND94–2585 • UC–814
Unlimited Release
Printed June 1995

Yucca Mountain Site Characterization Project

Creep in Topopah Spring Member Welded Tuff

R. J. Martin, III, R. H. Price, P. J. Boyd, J. S. Noel

Prepared by
Sandia National Laboratories
Albuquerque, New Mexico 87185 and Livermore, California 94550
for the United States Department of Energy
under Contract DE-AC04-94AL85000

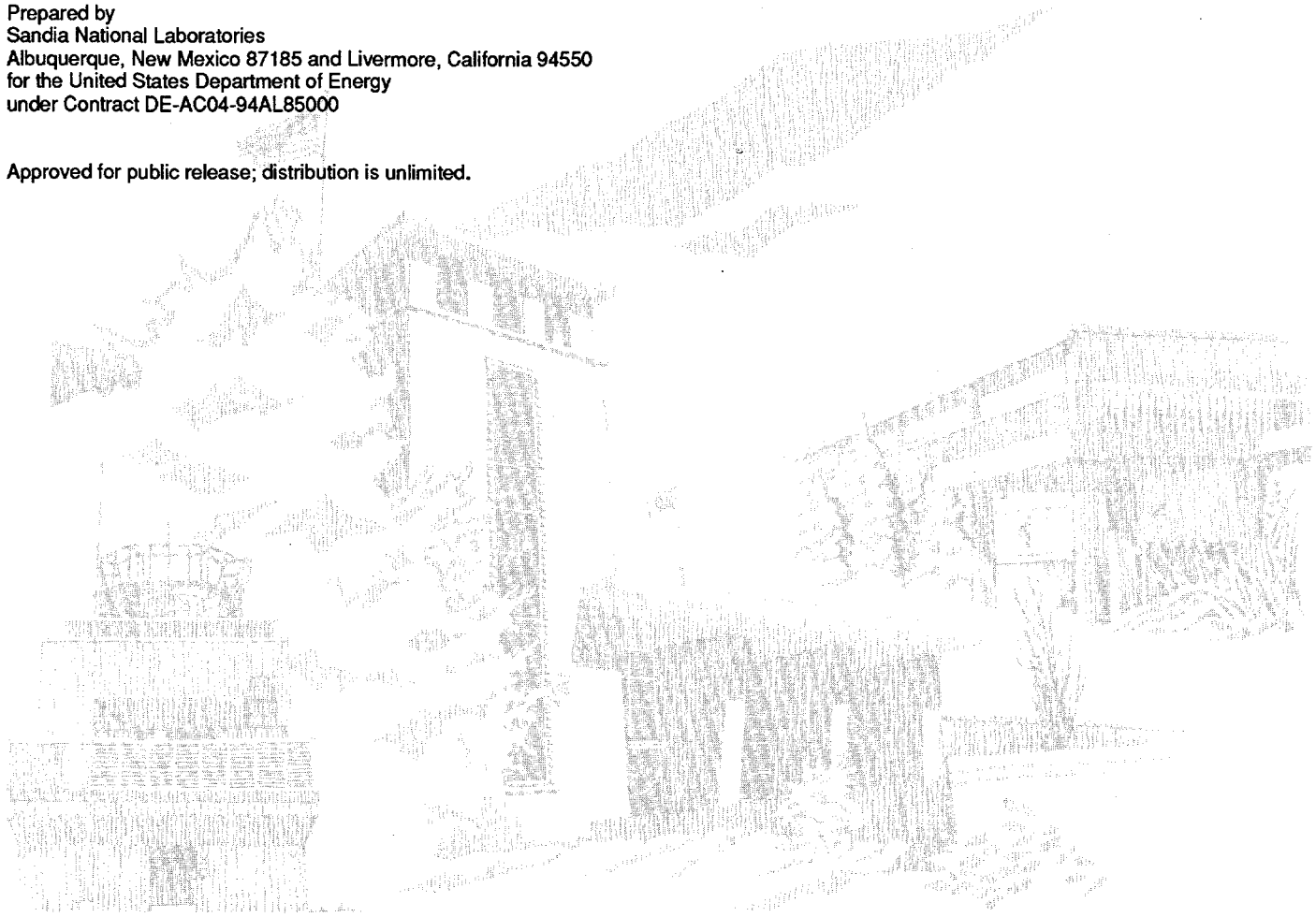

"Prepared by Yucca Mountain Site Characterization Project (YMSCP) participants as part of the Civilian Radioactive Waste Management Program (CRWM). The YMSCP is managed by the Yucca Mountain Project Office of the U.S. Department of Energy, DOE Field Office, Nevada (DOE/NV). YMSCP work is sponsored by the Office of Geologic Repositories (OGR) of the DOE Office of Civilian Radioactive Waste Management (OCRWM)."

Issued by Sandia National Laboratories, operated for the United States Department of Energy by Sandia Corporation.

Available to DOE and DOE contractors from
Office of Scientific and Technical Information
PO Box 62
Oak Ridge, TN 37831

Prices available from (615) 576-8401, FTS 626-8401

Available to the public from
National Technical Information Service
US Department of Commerce
5285 Port Royal Rd
Springfield, VA 22161

NTIS price codes
Printed copy: A04
Microfiche copy: A01

Distribution
Category UC-814

SAND94-2585
Unlimited Release
Printed June 1995

CREEP IN TOPOPAH SPRING MEMBER WELDED TUFF

R. J. Martin, III[1], R. H. Price[2], P. J. Boyd[1], J. S. Noel[1]

[1]New England Research, Inc.
White River Junction, Vermont 05001

[2]YMP Performance Assessment Applications Department
Sandia National Laboratories
Albuquerque, New Mexico 87185

ABSTRACT

A laboratory investigation has been carried out to determine the effects of elevated temperature and stress on the creep deformation of welded tuffs recovered from Busted Butte in the vicinity of Yucca Mountain, Nevada. Water saturated specimens of tuff from thermal/mechanical unit TSw2 were tested in creep at a confining pressure of 5.0 MPa, a pore pressure of 4.5 MPa, and temperatures of 25 and 250 °C. At each stress level the load was held constant for a minimum of 2.5×10^5 seconds and for as long as 1.8×10^6 seconds. One specimen was tested at a single stress of 80 MPa and a temperature of 250 °C. The sample failed after a short time. Subsequent experiments were initiated with an initial differential stress of 50 or 60 MPa; the stress was then increased in 10 MPa increments until failure. The data showed that creep deformation occurred in the form of time-dependent axial and radial strains, particularly beyond 90% of the unconfined, quasi-static fracture strength. There was little dilatancy associated with the deformation of the welded tuff at stresses below 90% of the fracture strength. Insufficient data have been collected in this preliminary study to determine the relationship between temperature, stress, creep deformation to failure, and total failure time at a fixed creep stress.

This report was prepared for the Yucca Mountain Site Characterization Project. The scientific investigation discussed in this report is covered under the description of work for WBS number 1.2.3.2.7.1.3, QA Grading Report #1.2.3.2.7.1.3, Revision 00. The planning documents that guided this work activity are Site Characterization Plan Section 8.3.1.15.1.3; Study Plan SP-8.3.1.15.1.3, Revision 0; and Work Agreement WA-0090. The information and data documented in this report were collected under a fully qualified QA Program and may be used in licensing the repository.

CONTENTS

List of Figures

List of Tables

1.0 INTRODUCTION

The applicability of laboratory data for engineering and modeling purposes is a prime concern for the design and licensing of the potential nuclear waste repository at Yucca Mountain, Nevada. The repository must be designed to handle canisters generating high thermal loads. Temperatures in excess of 200 °C may be generated in the vicinity of the emplaced waste. The thermal loading is expected to persist for hundreds of years and will generate induced stresses that may cause local failure of the rock. Consequently, it is important to examine the effect of temperature and stress on the long term behavior of the welded, lithophysal-poor zone tuff in the potential repository horizon.

Typically, rocks subjected to a constant load at elevated temperatures display creep behavior. Even brittle crystalline rock at temperatures well below its melting temperature exhibit this phenomena. Limited data exists in the literature for the creep deformation at elevated temperatures on welded tuff. Such data will be useful to the performance assessment of the potential repository and will be required as an integral part of the licensing procedure.

1.1 Creep in Brittle Rocks

In order to evaluate creep data on tuff, a review of earlier studies on creep in brittle rocks and the mechanisms responsible for the observed effects may prove beneficial. One of the most striking characteristics of brittle rocks is that at temperatures well below the melting point, a rock subjected to a constant load exhibits a continuous increase in strain with time. This time-dependent deformation is called creep. Studies on creep indicate that the observed strain depends upon the applied stress, the temperature, the partial pressure of water, and the confining pressure (Matsushima, 1960, Misra and Murrell, 1965; Rummel, 1969; Martin, 1972b; Peng, 1973; Kranz and Scholz, 1977). Moreover, the same mechanism responsible for the strain of brittle rocks in constant strain-rate tests is also

operative in creep. That is, cracking, both along grain boundaries and through individual grains, produces the observed strain (e.g., Brace, 1964; Brace et al., 1966; Scholz, 1968a; Wawersik, 1972).

Above approximately one half to two-thirds of the compressive strength, the dominant mode of deformation for brittle rocks is the opening and subsequent growth of axial cracks. The formation of cracks parallel to the axis of greatest compressive stress has been verified in several ways. Most notable is the inelastic increase in volume, called dilatancy, as the fracture strength is approached (Brace et al., 1966). In addition, experimental studies on cracks in glass and plastic plates have shown that inclined cracks do not extend in their own plane when the plate is loaded in compression, but form branch fractures at or near the ends of the inclined crack. These branch cracks grow along curved paths until they become parallel to the axis of compression (Brace and Bombolakis, 1963;). As the stress is increased, the cracks continue to extend stably in the direction of the greatest compression. Direct observation of crack orientations in polished sections of rocks tested in compression also shows a predominance of intracrystalline cracks parallel to the axis of compression above approximately 60% of the fracture strength (Wawersik, 1968; Peng, 1973). Finally, Brace and Riley (1971) conducted uniaxial strain experiments on several brittle rocks and found that, when axial cracking is inhibited, the rocks did not fail even when the axial stress exceeded 2,000 MPa.

1.2 Theory for Time-Dependent Crack Growth in Silicates

If time-dependent strains observed in brittle crystalline rocks are related to axial cracking, it might be asked, "Is there a basic time dependence associated with the formation and growth of axial cracks that may be related to creep?" One approach is to assume that axial cracks lengthen with time under a constant load and that the strain rate of rocks in creep is related to the time-dependent growth of these cracks.

Experimental results indicate that stable time-dependent crack-growth at a constant compressive load or at a constant stress intensity factor (in tension) occurs in quartz and glass in the presence of water vapor. Moreover, the rate of crack growth depends on the applied stress, the temperature, and the partial pressure of water in the atmosphere surrounding the crack. The relative weakening of quartz or silicate glass, reflected by an increase in the rate of crack growth with an increase in any of the three variables, is consistent with the general theory of stress corrosion in silicates proposed by Charles (1965). They postulated that the velocity of a slowly propagating crack with a high tensile stress at the crack tip is proportional to the rate of the hydration reaction at the crack tip. Wiederhorn (1968) quantified the relationship with the following general equation for environment-sensitive crack growth

$$v = v_0 \beta P^n \exp\left(\frac{\Delta F - V^* \sigma}{RT} + \frac{\gamma Vm}{\rho RT}\right) \qquad (1)$$

where v is the rate of crack growth, P is the partial pressure of water, ΔF is the activation energy for the process, T is temperature, R is the universal gas constant, V^* is the activation volume, σ is stress, γ is the surface energy of the solid, Vm is the molar volume of the solid, ρ is the radius of curvature of the crack tip, and β and n are constants.

The theory developed by Wiederhorn (1968) suggests that if the partial pressure of water, the temperature, and the applied stress (or stress intensity factor) are constant, a constant crack propagation velocity will be observed. When any one of the thermodynamic variables is increased, the crack velocity increases. This expression has been verified through a number of experimental studies (Wiederhorn, 1968; Martin, 1972a; Scholz, 1972; Martin and Durham, 1975; Dunning et al., 1978; Atkinson, 1984).

1.3 Creep in Low Porosity Rocks

Next, let us examine the behavior of brittle rocks during creep and then compare these observations with the results of stable, time-dependent crack growth. Typically, creep is reported in terms of three distinct phases: primary or transient creep, secondary or steady-state creep, and tertiary or accelerating creep.

Transient creep has been reported for a variety of rock types over a wide range of temperatures and pressures (Lomnitz, 1956; Matsushima, 1960, Misra and Murrell, 1965; Rummel, 1969; Kranz and Scholz, 1977). The strain in this region decelerates rapidly and is often reported as proportional to the logarithm of time. Moreover, both the lateral and the longitudinal strains exhibit this logarithmic time dependence.

At low stresses, transient creep may account for the observed strain. However, at high stresses, secondary creep is often observed. Generally, in secondary creep, often called steady-state creep, the strain is proportional to time. The total strain caused by both primary and secondary creep is often represented by an equation of the form

$$\varepsilon = A + B \log t + Ct \qquad (2)$$

where ε is strain, t is time, and A, B, and C are constants.

Examples of primary and secondary creep observed in a biotite granite are shown in Figure 1. Constant stresses of 88 and 98 MPa were applied to biotite granite specimens. Shortly after the application of the load, a high strain rate, decreasing with time, is observed. Above approximately 2×10^4 seconds, the strain rate is nearly constant; this is interpreted as secondary creep. With increasing applied load, both the magnitude of the observed strain and the strain rate increased. These data are consistent with the empirical behavior described in Equation 2.

If secondary creep is allowed to continue, eventually the strain rate increases

(tertiary creep) and the rock fails. All three stages of creep have been observed in granite, quartzite, diabase, and granodiorite (Lomnitz, 1956; Matsushima, 1960, Rummel, 1969; Martin, 1972a; Kranz and Scholz, 1977; Martin et al., 1978). A short-term creep experiment conducted by Martin et al., (1978) on Ralston diabase shows the three stages of creep distinctly. The volumetric strain observed on a right-circular cylinder of diabase subjected to a confining pressure of 50 MPa and a fixed differential stress of 548 MPa is shown as a function of time in Figure 2. The specimen failed approximately 1200 seconds after the application of the load. The three regions are shown for illustrative purposes: the primary creep region: 0 - 250 seconds; the secondary creep region: 250 to approximately 900 seconds; and the tertiary creep region: the rapid acceleration of volumetric strain culminating in failure.

1.4 Time Dependent Crack Growth as a Mechanism for Creep

Stable crack growth in quartz reported by Martin (1972a), Martin and Durham, (1975), and Dunning et al., (1975) illustrated specific characteristics that are related to creep deformation. In these studies, the specimens were loaded to a fixed compressive stress and the growth of a crack parallel to the applied load was observed. The crack was initiated by drilling a small hole through the center of the specimen to act as a stress concentrator to initiate the crack. Each specimen was tested in a controlled environment and the change in crack length was noted as a function of time. A typical data set obtained on a single specimen of quartz tested at a temperature of 241 ^{o}C and a partial pressure of water of 4.5×10^{-2} kPa is shown in Figure 3. The test specimen geometry is shown in the upper left portion of the graph. At a stress of 66 MPa, the change in crack length with time is very similar to that observed in the creep data shown in Figures 1 and 2. First, the crack exhibits an initial period of rapidly decelerating growth followed by a quasi-linear or secondary segment. After 6.3×10^{4} seconds, the stress was increased to 74 MPa.

Immediately the rate of crack growth increased. The same characteristics observed at the lower stress were exhibited for the 74 MPa segment. Initially there was a strong transient followed by a secondary or quasi-linear crack growth segment. After approximately 8 x 10^4 seconds, the stress was increased to 83 MPa. The rate of crack growth increased dramatically, but continued to decrease until the experiment was terminated when the crack length reached 3.7 mm.

These data are consistent with the effects predicted by Equation 1; that is, the rate of crack growth increased with increasing stress and nearly vanishes at low stresses. Additional experiments showed that increasing either the partial pressure of water surrounding the crack or the temperature also results in an increase in the rate of crack growth. The characteristics of the change in crack length with time are very similar to those shown in Figure 3.

Equation 1 predicts crack growth at a constant velocity. This is not observed in the specimens tested where the applied load is compressive. Several reasons have been suggested to explain this behavior. First, the partial pressure of water at the crack tip decreases as the crack length increases. Propagation occurs when hydration reaction alters the covalent Si-O bonds to form weaker Si-OH Van der Waal type bonds. This reaction produces a volume increase, which reduces the diffusivity along the path to the crack tip. The net effect is a reduction of the partial pressure of water at the crack tip, which inhibits growth. It is important to note the rate of the hydration reaction is dependent on the partial pressure of water at the crack tip. Second, the stress intensity factor at the crack tip decreases with increasing crack length.

The similarity in form between the creep curve and that for time-dependent crack growth is in itself not sufficient to conclude that crack growth is the mechanism of creep in brittle rocks. What is needed is a theory of creep that defines the observed strain in terms of time-dependent crack growth. Martin (1972a) showed that for randomly oriented

cracks, the strain-rate of a rock in creep is proportional to the rate of crack growth. If the only effect of increasing the temperature, stress, or partial pressure of water was to augment the rate of crack growth on pre-existing cracks, the same dependencies for an isolated crack in quartz should closely approximate those in brittle silicate rocks.

An alternative approach is to consider a model based on the time required for a crack to extend to a critical length and not consider the details of propagation. Scholz (1968b) has successfully demonstrated that creep can be treated statistically as the static fatigue of independent regions throughout the rock. Static fatigue refers to the failure time of a rock or single crystal at constant stress, temperature, confining pressure, and partial pressure of water without regard to the strain history. Scholz (1972) conducted a series of static fatigue tests in compression on single crystal quartz. He observed that the mean time to failure, $\langle t \rangle$, depended on the partial pressure of water, P; stress, σ; and temperature, T, according to

$$\langle t \rangle = t_o P^{-a} \exp \left(\frac{\Delta F}{RT} - K' \sigma \right) \qquad (3)$$

where a and K' are constants.

Figure 4 shows the constant compressive stress applied to single crystals of quartz loaded at room temperature as a function of the time to failure (Scholz, 1972). At high stresses (approaching 2,100 MPa) the time to failure is less than 10 seconds. For specimens tested at lower stresses, the time to failure increases. For example, at stresses near 1,500 MPa fracture times range between 10^4 and 10^6 seconds. The functional relationship between stress and failure time is consistent with the general form of the equation given in Equation 1. Additional experiments showed the time to failure decreased with increasing temperature at a constant stress and constant partial pressure of water. Once again, these phenomena are consistent with moisture-assisted, time-dependent crack growth.

The foregoing discussion demonstrates that the strength of brittle, silicate rocks is not a single-valued function of any parameter, but is a complex continuum that depends on the state of stress, the saturation (pore pressure), the temperature, and the time (including strain rate). To further complicate the matrix, once these parameters have been determined at one scale, there is a volume dependence that has to be taken into account. Price (1987) has shown that strength is a function of size for specimens of Topopah Spring Member welded tuff with diameters less than 230 mm. Since the potential nuclear waste repository at Yucca Mountain will be subjected to uncommon conditions, it seems prudent to bound the behavior and long-term strength of the tuff. It will be of particular interest to know how the strength of tuff varies with temperature, stress, and saturation. If the repository is to experience temperatures in excess of 200 ^{o}C, the strength of the rock probably will be degraded. Furthermore, changes in saturation will have an impact on the strength. Finally, because the repository will experience thermally induced stresses for a significant portion of its design life, it is necessary to quantify the effect of this long-term loading on time-dependent deformation (creep).

1.5 Behavior of Welded Tuff

A large number of deformation experiments have been carried out to determine the elastic and fracture properties of the Topopah Spring Member tuff. Special interest has been given to the TSw2 thermal/mechanical unit, the potential repository horizon. In this study, we are interested in the strength and deformation characteristics of this welded tuff. Typical stress-strain curves measured in uniaxial compression for two specimens recovered from borehole USW-NRG-7/7A, selected to show key aspects of the behavior, are shown in Figures 5 and 6. Both specimens had very similar dry bulk densities, grain densities, and porosities. The porosity of the specimen recovered from 1259.1 feet was 9.8%, while that of the specimen recovered from 1265.2 feet was 9.6%. The data were collected on

saturated specimens tested in uniaxial compression at a strain rate of 10^{-5} s^{-1}. Axial stress and radial strain are plotted as functions of axial strain in the upper two graphs. Axial strain is plotted as a function of time in the lower left graph, and axial stress is plotted as a function of volumetric strain in the lower right portion of the figures. The strength of both rocks is very similar (in excess of 170 MPa). The axial stress versus axial strain curve is extremely linear to failure. In contrast, the slope of the radial versus axial strain curve is concave upward. This suggests that the deformation is not totally elastic and some microcrack development is occurring. This is more clearly seen by examining the axial stress versus volumetric strain curves. Both specimens exhibit some dilatancy; however, the magnitude of the inelastic volumetric strain is quite different. Specimen 1259.1 displayed little dilatancy, whereas the dilatancy in 1265.2 was pronounced. Furthermore, the onset of dilatancy occurs at approximately 60% of the fracture strength for 1265.2 and closer to 90% of the fracture strength for 1259.1. Examination of many TSw2 specimens tested under similar conditions shows that the more characteristic behavior is that exhibited by 1259.1; that is, the deformation is characterized by very little dilatancy, and what dilatancy is observed occurs late in the loading history. These observations are consistent with similar measurements on other welded tuff. Scholz (1968a) also tested welded tuff. He observed that the dilatancy measured during loading was much smaller than that typical of other low porosity brittle rocks such as quartzite, sandstone, and granite.

These results suggest that the dilatancy observed in other low porosity crystalline rocks (e.g. Brace et al., 1986; Scholz, 1968a) is not a characteristic of TSw2. The implication is that the interaction of a large number of microcracks that produce a nonlinear increase in the radial strain normal to the loading axis, above approximately half of the compressive stress, is not operative in welded tuff. Rather, it appears that axial cracks develop during deformation and propagate in their own plane, at least partially, until the ultimate strength of the rock is very nearly achieved. This hypothesis is substantiated by

observing the nature of the fractured rock. In most cases, the rock fails catastrophically through a series of extension fractures often propagating through the ends of the specimen.

It is also possible that axial cracks form late in the loading history (approaching 90% of the fracture strength) over a narrow range of nucleation stresses. In this case crack interaction, producing dilatancy, would not occur until the final stages of the failure process. In the absence of simultaneous acoustic emission measurements, there is no definitive way to determine the onset of axial cracking and the interaction of propagating cracks.

Another possible reason for the small observed dilatancy in welded tuff is the compaction of pores offsetting the increase in volume due to microcrack development. Pore crushing and compaction does not appear prevalent in the welded units of the Topopah Spring Member tuff. Linear compressibility was measured to pressures of 50 MPa; the pressure versus strain curves were linear (Martin et. al., 1992). Furthermore, the hysteresis in the pressure versus strain data was small and no permanent compaction was observed at the conclusion of the pressurization cycle. In addition, several specimens of TSw2 from Busted Butte, tested in both unconfined and confined compression, have been unloaded prior to failure. For these specimens, very little hysteresis in the stress versus strain data was observed during unloading. These observations indicated that pore compaction and crushing is not dominant in welded tuff.

In light of the fact that welded tuff exhibits a behavior that is somewhat different from other low porosity crystalline rocks, it is possible that the creep strains, at a constant stress, observed in previous studies of creep in crystalline rock (Lomnitz, 1956; Matsushima, 1960, Wawersik, 1972; Martin, 1972; Cruden, 1974; Kranz and Scholz, 1977; Martin, et al., 1978) may not be as pronounced in tuff, while the time to failure may still depend on temperature, stress, and water saturation.

In order to investigate the creep behavior of tuff from the potential repository

horizon at Yucca Mountain, several creep experiments have been performed. Each test was carried out on a saturated specimen of welded tuff at a confining pressure of 5.0 MPa, a pore pressure of 4.5 MPa, temperatures of 25 and 250 °C, and differential axial stresses ranging from 50 to 130 MPa.

2.0 EXPERIMENTAL SET-UP

Creep experiments were conducted on welded tuff cores recovered from Busted Butte in the vicinity of Yucca Mountain, Nevada. The specimens were cored from large boulders of the Topopah Spring Member tuff (thermal/mechanical unit TSw2). TSw2 is a lithophysal poor welded tuff and is the potential repository horizon. Busted Butte specimens were utilized because of their availability and close similarity to borehole specimens recovered within the potential repository block (Price et al., 1987). The physical characteristics of the specimens are given in Table 1. Ground right circular cylinders 50.8 mm in diameter and 101.6 mm in length were prepared. Prior to testing, the dry bulk density, saturated bulk density, porosity, and compressional and shear wave velocities (parallel and normal to the axis) were measured. A detailed description of the sample procedure and set up is given by Martin et al. (1993).

For the high temperature experiments, a simple polyolefin jacket was not suitable. Consequently, the sample was positioned between low thermal conductivity Macor ceramic spacers, and the entire sample assembly (i.e., tuff specimen and Macor spacers) was jacketed with 0.13 mm thick copper. The jacketed sample was then swaged onto a stainless steel plug to seal the jacket and isolate the sample from the confining medium. Once the sample was positioned on the base plug of the pressure vessel, the furnace was lowered into place, and the LVDTs used to measure axial and radial deformation were connected to the electrical feed-throughs and checked for continuity. Figure 7 shows a schematic diagram of the sample assembly, furnace, and pressure vessel used for the

measurements.

The furnace used in these experiments has two zones with independent controls and feedback thermocouples. The thermocouple for the lower zone is located in the pore pressure inlet tube and senses the temperature at the bottom of the tuff specimen. The upper zone of the furnace is monitored with a thermocouple that enters the pressure vessel through the loading piston and impinges on the top of the sample assembly. A calibration sequence was carried out prior to initiating the high temperature experiments to determine the power required by each zone to develop a temperature of 250 °C with a gradient along the axis of the sample of less than ±4 °C.

The jacketed sample was instrumented to measure the axial and radial displacement during loading. LVDTs were used to monitor the change in sample geometry. Because of the high temperature, it was necessary to locate the axial LVDTs near the base plug of the system to remove them from the temperatures encountered within the furnace assembly. To accomplish this, the LVDT barrels were supported in extended tubes attached to the lower ends of the sample (see Figure 6). The cores were secured on extended stainless steel rods mounted in a second ring located near the top of the sample. The extension rods for the cores passed through the tubes supporting the LVDT barrels and into the transducer.

The radial strain was measured with a radial displacement gage very similar to that described in Holcomb and McNamee (1984) with the support ring for the LVDT located outside the furnace assembly. Radial gage access to the sample was achieved by passing the extension rods through holes in the wall of the furnace. The LVDT core was coupled to the rock with an extended rod that passed through the furnace wall. The most important consideration in this arrangement is the isolation of the LVDT barrels from the high temperatures inside the furnace. The temperature experienced by the LVDTs did not exceed 105 °C. Thermocouples were positioned next to the LVDTs to monitor the temperature.

The creep tests were carried out in a servo-controlled hydraulic loading frame with

an axial load capacity of 1.1×10^6 N. The system was operated in force feedback; the outputs from seven transducers (three LVDTs, two load cells, a ram displacement gage, and a thermocouple) were amplified and recorded in a computer-based data-acquisition system.

Following an initial check of all the electrical connections, the confining pressure was increased to 5.0 MPa. The confining medium was argon. After the confining pressure stabilized and no leaks in the jacket were detected, the pore pressure was increased to 4.5 MPa. Once the pore pressure was in equilibrium, the sample was heated to 250 °C at a rate not exceeding 2.0 °C per minute. During the heating and differential-stress loading phases of the experiment, the confining pressure and pore pressure were held constant with servo-controlled intensifiers.

The constant stress experiment was carried out in stages. First the confining and pore pressures were applied. Then the temperature of the specimen was established. Once the sample and test apparatus were in thermal equilibrium, a differential axial stress was applied to the specimen at a constant stress rate. The differential axial stress was held constant and the deformation of the specimen was observed. If no significant axial shortening of the specimen was observed (i.e., the strain rate was less than 10^{-9} s^{-1}), the stress was increased by 10 MPa. This process was continued until the specimen failed or the experiment was terminated. This method was used to evaluate the creep response of the tuff at various levels in a reconnaissance fashion. These tests are primarily scoping in purpose. Future test will adhere to conventional ASTM procedures.

Once a specimen failed it was removed from the apparatus and examined. Particular interest was paid to the mode of failure and the condition of the jacket when the specimen was removed.

3.0 EXPERIMENTAL RESULTS

3.1 Ambient Temperature Creep

Data for a typical experiment performed at ambient temperature are shown in Figures 8a, 8b, 8c, 8d, and 8e. Figure 8a shows the stress history for specimen BB-10AE-36Z-SNL. An initial differential axial stress of 50 MPa was applied to the specimen. At periodic intervals the stress was increased to 60, 70, and finally 80 MPa. After a cumulative duration of 1.45×10^6 seconds the specimen was unloaded.

The axial strain measured as a function of time is shown in Figure 8b. The strain increased stepwise as the applied stress was increased. The large majority of the deformation occurred during the loading of the specimen. Minimal time-dependent axial strain was noted during the constant stress segments of the time history. The time-dependent deformation occurred almost exclusively as transient creep.

If the time history is neglected and the strain is plotted as a function of the applied load, a stress-strain curve similar to those recorded for constant strain rate experiments can be plotted. These constructions are shown in Figures 8c, 8d, and 8e. Figure 8c shows differential axial stress plotted as a function of axial strain for both the uploading and downloading sequence on the specimen. The curve is linear to a peak differential axial stress of 80 MPa. These data are very similar to those shown in Figures 5 and 6 for the constant strain rate experiments. Radial strain is plotted as a function of axial strain in Figure 8d. The loading curve is broken by offset segments, whereas the downloading portion of the curve is nearly linear. The offsets in the radial strain are most likely caused by the nature of the radial gage used in the experiments. The radial gage protrudes through the furnace to contact the specimen. The offsets coincided with the incremental loading of the specimen. Neglecting the offsets, the data are similar to those reported for constant strain rate experiments on TSw2, at stresses below approximately one half of the fracture strength. Finally, differential

axial stress is plotted as a function of volumetric strain in Figure 8e. The curve is nearly linear to the peak differential stress of 80 MPa. The unloading curve is linear and only a small amount of permanent strain (about 0.1 milli or 10^{-4}) is observed at the conclusion of the experiment.

A second ambient temperature creep experiment is shown in Figures 9a to 9f. Figure 9a shows the loading history of the specimen. An initial 50 MPa differential axial stress was applied to the specimen. The load on the specimen was incremented by 10 MPa at intervals of approximately 5.2×10^5 to 1.4×10^6 seconds until the rock failed at a differential axial stress of 130 MPa. The total duration of the experiment was 6.8×10^6 seconds (almost 79 days). Figure 9b shows the change in axial strain as a function of time. At low stresses (below 100 MPa), almost all of the strain accumulation occurs during the incremental loading. The strain rate during the constant stress portion of the time history is less than 10^{-9} s^{-1}. After the stress was increased to 110 MPa, a small axial strain rate was detected. With subsequent stress increases to 120 MPa and finally 130 MPa, the strain rate during the constant stress portion of the curve increased further. The most pronounced strain rate (1.3×10^{-9} s^{-1}) occurred during the 130 MPa segment just prior to failure. The radial strain is plotted as a function of time in Figure 9c. The behavior of the radial strain is very similar to that of the axial strain. That is, at differential axial stresses below 100 MPa the strain accumulation occurred during incremental loading; no measurable strain accumulated during the constant stress segments. However, above 100 MPa the radial strain increased with time and the strain rate was greater with each subsequent stress increment.

As with specimen BB-10AE-36Z-SNL, these data can be plotted as conventional stress-strain curves. Figure 9d presents the differential axial stress plotted as a function of axial strain. The stress-strain curve exhibits an offset in the axial strain corresponding to the creep episodes at each stress level, with the offsets being pronounced for creep stresses of 100, 110, 120, and 130 MPa. Similarly, the radial strain is plotted as a function of axial

strain in Figure 9e. The characteristics of the curve are similar to those in a constant strain rate experiment. The small offsets in the radial strain occur as failure is approached, which corresponds to the creep episodes as shown in Figures 9b and c. Figure 9f presents the differential axial stress as a function of volumetric strain. The curve is more or less linear to approximately 120 MPa; the sample dilates at a stress of 130 MPa. The curve is very similar to that shown in Figure 5 for the TSw2 specimen tested from borehole USW NRG-7/7A at a depth of 1259.1 feet.

3.2 High Temperature Creep

Specimen BB-10AE-22Y-SNL was initially tested in creep at a differential axial stress of 80 MPa. After the specimen was unloaded, the temperature was increased and the specimen was tested once again at a temperature of 250 °C. The confining and pore pressures were the same as for the room temperature conditions; the confining pressure was 5.0 MPa, and the pore pressure was 4.5 MPa. The stress-time history for the high temperature segment of the experiment is shown in Figure 10a. Figure 10b shows the change in axial strain with time. Several high frequency cycles are observed at times near 1×10^4, 3×10^4, and 6×10^4 seconds. An examination of the axial strain, radial strain, confining pressure, temperature, and stress data show a consistent pattern. The oscillations were precipitated by small fluctuations in the confining pressure with a maximum peak-to-peak value of 0.047 MPa. With a gas confining medium, the intensification system is very soft and purposefully has a sluggish response. Once the servo-control loop went into oscillation, the confining pressure triggered a change in the convection pattern within the test chamber resulting in a temperature fluctuation of ± 3 °C. The combined pressure and temperature variations produced thermal expansion and hydrostatic compression of the support rings for the axial and radial LVDTs. The net effect was an apparent strain change in the tuff specimen. Clearly, some strain is associated with these changes. However, the

magnitude of the strain experienced by the rock is smaller than that reported in Figure 10. Furthermore, the stress on the specimen and the axial displacement measured outside the pressure vessel showed no change.

The specimen quickly failed approximately 6.1×10^4 seconds after loading (about 17 hours). Figure 10c shows radial strain as a function of time. Most of the strain accumulation in the radial direction occurred during initial loading and at the failure of the specimen. After load was applied for approximately 5.5×10^4 seconds, the radial strain remains more or less constant. Beyond that point there is a gradual increase in radial strain culminating in failure.

Conventional stress-strain curves were also plotted using the creep data. Differential axial stress is plotted as a function of axial strain in Figure 10d. The curve is linear up to a differential axial stress of 79 MPa. This represents the initial constant nominal stress rate of 2 MPa s^{-1} loading segment of the experiment. The increase in strain at a constant stress of 79 MPa represents the creep episode. The cumulative radial strain is plotted as a function of axial strain in Figure 10e. The curve is slightly concave upward, with rapid accumulation of radial strain at failure. The differential axial stress is plotted as a function of volumetric strain in Figure 10f. The curve is nearly linear up to failure. No dilatancy is observed in these data.

The high temperature portion of an experiment on specimen BB-10AE-36Z-SNL is shown in Figures 11a to 11e. After the ambient portion of the experiment was complete, the temperature was increased to 250 ^{o}C at a confining pressure of 5.0 MPa and a pore pressure of 4.5 MPa. Figure 11a shows the stress-strain time history. The differential axial stress on the specimen was increased to approximately 58 MPa and held constant. After approximately 5×10^5 seconds (almost 6 days), the differential axial stress was increased to 69 MPa and subsequently to 79 MPa. The experiment was terminated after 3.2×10^6 seconds (over 37 days) because of a furnace failure. The specimen did not fail.

Axial strain is plotted as a function of time in Figure 11b. As with the previous experiments, the greatest strain accumulation occurs during loading and subsequent increases in axial stress. However, a small, but significant strain accumulation occurred at each of the constant stress segments; the strain rate was on the order of 10^{-10} s^{-1}. In spite of the somewhat noisy data, the increase in axial strain is very apparent in Figure 11b. The radial strain transducer was noisy and reliable data could only be obtained for the first loading increment.

A conventional stress-strain curve for the high temperature portion of the experiment is shown in Figure 11c. Offsets in the axial strain at fixed axial stress represent the strain accumulation during creep episodes. These data show pronounced creep strain accumulation at stresses of 58, 69, and 79 MPa; however, the slope of the stress-strain curve is the same for each stress increase. Figure 11d shows radial strain as a function of axial strain during the constant strain rate loading of the specimen to 58 MPa. These data can be used to obtain the high temperature Poisson's ratio. The volumetric strain is shown as a function of differential axial stress for the constant strain rate loading to 58 MPa in Figure 11e. The curve is linear with no inelastic volumetric strain.

4.0 DISCUSSION

The creep experiments on specimens of Topopah Spring Member tuff from thermal/mechanical unit TSw2 show that creep deformation occurs in the form of time-dependent axial and radial strain, particularly at stresses above 90% of the uniaxial compressive strength. This behavior is observed both at ambient and elevated temperatures.

The small inelastic volumetric strain accumulation during the entire test may indicate that cracks propagating at a constant axial stress do not interact with other cracks to produce a significant dilatancy. The mode of failure in these specimens is, in most cases,

dominated by axial through-going (or extension-type) fractures. This further suggests that the small micro-cracks characteristic of other low porosity crystalline rocks such as quartzites, granites, and diabases do not occur in tuff.

Because of the nature of the loading history of these specimens, it is difficult to determine the effect of temperature on the time to failure in creep. The stress to produce failure appears to decrease with increasing temperature, although there are insufficient data to quantify the effect. Additional data will be required to refine this effect because as we have seen in other studies the strength of tuff observed in constant strain rate experiments at ambient temperature can vary by as much as a factor of two within thermal/mechanical unit TSw2 (e.g., Martin et al., 1994).

The data collected here are consistent with a creep mechanism of time-dependent crack growth. Strain rates observed at stresses approaching the uniaxial compressive strength increase with increasing stress. Unfortunately, the limited amount of data do not permit further comparisons between the observed strain rates and time to failure at constant load as a function of temperature. The data do, however, indicate that the temperature causes a reduction in strength.

An additional confirmation for the stress-corrosion cracking mechanism is indicated by the results of constant strain rate experiments on specimens of TSw2 (Martin et al., 1993). These data are shown in Figure 12. The strength of saturated tuff specimens tested in uniaxial compression is plotted as a function of the strain rate. As the strain rate was decreased from 10^{-5} to 10^{-9} s^{-1}, the strength decreased. At strain rates near 10^{-5} s^{-1}, the strengths ranged from 100 to 160 MPa. In contrast, the strengths at a strain rate of 10^{-9} s^{-1} varied between 45 to 108 MPa. The decrease in strength with decreasing strain rate is consistent with the stress corrosion cracking mechanism. Martin (1972) proposed a time-dependent crack mechanism for the decrease in rock strength with decreasing strain rate. The velocity of crack propagation in silicates for a wide variety of loading geometries

is dependent on the applied stress (or stress intensity factor), the partial pressure of water at the crack tip, and the temperature. A constant strain rate experiment can be idealized as a series of incremental loading sequences to successively higher stresses with the duration of the intervals increasing with decreasing strain rate. The degradation in strength with decreasing strain rate is approximately 28% per thousand fold decrease in strain rate.

The strength of rock does not decrease indefinitely with decreasing strain rate. Neither do brittle silicate rocks creep to failure at vanishingly low differential stresses. There must be some lower limit for the strength of rocks. Obviously this limit will depend on temperature and saturation that the rock is experiencing. Costin (1983) proposed a lower limit for the decrease in strength with decreasing strain rate. His model is based on linear fracture mechanics and stress corrosion cracking. He suggested that, at low strain rates, stress corrosion completely relaxes the tensile stresses at the crack tip and arrests crack growth. He calculated a critical strain rate of 10^{-9} s^{-1} for Westerly granite at ambient temperature for laboratory scale specimens; no data exit to verify this prediction. The data collected on tuff do not extend to sufficiently low strain rates to test the Costin's hypothesis. In terms of the current creep tests, Costin's model predicts that the long-term strength of tuff will decrease with increasing temperature. What is not clear is where the long-term strength reaches a lower limit as a result of the relaxation of stresses at the tips of propagating cracks.

The data on welded tuff are consistent with a stress corrosion cracking mechanism for the deformation and failure. These results suggest that the strength and creep deformation of tuff should be studied as a function of temperature, saturation, and applied load. In light of this, it seems prudent to conduct a series of constant stress experiments at elevated temperatures to map out the fracture strength as a function of time and temperature. These creep experiments will be used to constrain the long-term strength of the potential repository tuffs under high thermal loads.

5.0 REFERENCES

Atkinson, B. K., "Subcritical crack growth in geological materials," *J. Geophys. Res.*, v. 89, p. 4077-4114, 1984. (NNA.890928.0105)

Brace, W.F., and E.G. Bombolakis, "A note on brittle crack growth in compression," *J. Geophys. Res.*, v. 68, p. 3709-3713, 1963. (MOL.19950329.0285)

Brace, W.F., B.W. Paulding, Jr., and C.H. Scholz, "Dilatancy in the fracture of crystalline rocks," *J. Geophys. Res.*, v. 71, p. 3939-3953, 1966. (MOL.19940805.0099)

Costin, L.S., "A microcrack model for the deformation and failure of brittle rock," *J. Geophys. Res*, 88 (11), p. 9485-9492, 1983. (HQS.880517.1623)

Charles, R.J. , "The strength of silicate glasses and some crystalline oxides, high strength materials," John Wiley, New York, 1965. (NNA.930414.0029)

Dunning, J. D., W.L. Lewis, and D.E. Dunn, "Chemomechanical weakening in the presence of surfactants," *J. Geophys. Res.*, v. 85, p. 5344-5354, 1980. (MOL.19950411.0231)

Holcomb, D.J., and M.J. McNamee, "Displacement gage for the rock mechanics laboratory," *SAND84-0651*, Sandia National Laboratories, 1984. (NNA.910523.0022)

Lomnitz, C., "Creep measurements in igneous rocks," *J. Geol.*, 64, p. 473-479, 1956. (MOL.19950329.0284)

Martin, R.J., III, "Time-dependent crack growth in quartz and its application to the creep of rocks," *J. Geophys. Res.*, v.77, p. 1406, 1972a. (NNA.930215.0045)

Martin, R.J., III, "Static fatigue and creep of quartzite," *Eos Trans., AGU*, 53(4), p. 515, 1972b. (MOL.19950329.0266)

Martin, R.J., III and W.B. Durham, "Mechanisms of crack growth in quartz," *J. Geophys. Res.*, v. 80, p. 4837, 1975. (NNA.930215.0046)

Martin, R. J., III, R.E. Habermann, and M. Wyss, "The effects of stress cycling and inelastic volumetric strain on remanent magnetization," *J. Geophys. Res.*, v. 83, p. 3485, 1978. (MOL.19950329.0267)

Martin, R.J., III, R.H. Price, P.J. Boyd, and R. W. Haupt, "Anisotropy of the topopah spring member welded tuff," *SAND91-0894,* Sandia National Laboratories, 1992. (NNA.920522.0041)

Martin, R.J., III, R.H. Price, P.J. Boyd, and J. S. Noel, "The influence of strain rate and sample inhomogeneity on the moduli and strength of welded tuff," *Int. J. Rock Mech. Min. Sci. & Geomech. Abstr.* 15 (7), p. 1507-1510, 1993. (NNA.930514.0013)

Martin, R.J., III, R.H. Price, P.J. Boyd, and J.S. Noel, "Bulk and mechanical properties of the paintbrush tuff recovered from borehole USW NRG-6: data report, *SAND93-4020*, Sandia National Laboratories, 1994. (MOL.19940811.0001)

Matsushima, S., "On the flow and fracture of igneous rocks," *Disaster Prevention Res. Inst., Kyoto Univ. Bull,* 36, pp. 2-9, 1960. (MOL.19950411.0234)

Peng, Syh-Deng, "Time-dependent aspects of rock behavior as measured by a servocontrolled hydraulic testing machine," *Int. J. Rock Mech. Min. Sci. & Geomech. Abstr.* V. 10, p. 235-246, 1973. (MOL.19950411.0232)

Price, R.H., "Effects of sample size on the mechanical behavior of topopah spring tuff," *SAND85-0709*, Sandia National Laboratories, 1986. (NNA.891106.0125)

Price, R.H., J.R. Connolly, and K. Keil, "Petrologic and mechanical properties of outcrop samples of the welded, devitrified topopah spring member of the paintbrush tuff," SAND86-1131, Sandia National Laboratories, 1987. (HQS.880517.1704)

Riley, D.K. and Brace, W.F., "Uniaxial strain behavior of fifteen rocks to 30 kb" (abstract), *Eos Trans., AGU*, 52(9), p. 346, 1971. (MOL.19950329.0265)

Rummel, F., "Studies of time-dependent deformation of some granite and eclogite samples under uniaxial, constant compressive stress and temperatures up to 400° C," *J. Geophys.*, 35, p. 17-42, 1969. (MOL.19950206.0033)

Scholz, C.H., "Microfracturing and the inelastic deformation of rock in compression," *J. Geophys. Res.*, v.73, p. 1417, 1968a. (MOL.19950329.0269)

Scholz, C.H., "Mechanism of creep in brittle rock," *J. Geophys. Res.*, v 73, p. 3295, 1968b. (MOL.19950329.0270)

Scholz, C.H., "Static fatigue of quartz," *J. Geophys. Res.*, v.77 (11), p. 2104, 1972. (NNA.930224.0064)

Wawersik, W.R., "Time-dependent rock behavior in uniaxial compression," in *Proceedings of the 14th Symposium on Rock Mechanics*, p 85-106, Pennsylvania State University, University Park, PA, 1972. (NNA.890713.0229)

Wiederhorn, S. M., "Moisture assisted crack growth in ceramics," *Int. J. Fracture Mech,* 4 (2), p. 171-177, 1968. (NNA.930215.0036)

Table 1 Tuff Data Summary

Sample ID	BB-10AE-22Y-SNL	BB-10AE-36Z-SNL	BB-9394-SNL-A
Dry ρ_b (g/cm^3)1	2.29	2.32	2.30
Saturated ρ_b (g/cm^3)	2.38	2.40	2.38
Porosity (%)	9.3	8.0	8.1
Saturated P-Wave Velocity (km/s)	4.649	4.665	4.597
Saturated S1-Wave Velocity (km/s)	2.567	2.873	3.112
Saturated S2-Wave Velocity (km/s)	2.562	2.867	2.851
AMBIENT TEMPERATURE:			
Maximum Differential Axial Stress (MPa)	80.0	80.1	128.8 (Failure)
Duration at Maximum Differential Axial Stress (hours)	168	167	74
Cumulative Experiment Duration (hours)	168	404	1920
Static E (GPa)2	34.7	44.0	35.9
Static υ2	0.14	0.18	0.18
ELEVATED TEMPERATURE:			
Maximum Differential Axial Stress (MPa)	77.7	78.9 (No Failure)	N/A
Duration at Maximum Differential Axial Stress (hours)	17	241	N/A
Cumulative Experiment Duration (hours)	17	888	N/A
Temperature (°C)	250°	250°	N/A
Static E (GPa)2	36.9	39.7	N/A
Static υ2	0.03	0.17	N/A

1 ρ_b = Bulk density
2 υ = Poisson's ratio / E = Young's modulus (between 10% to 50% of maximum dfferential axial stress)

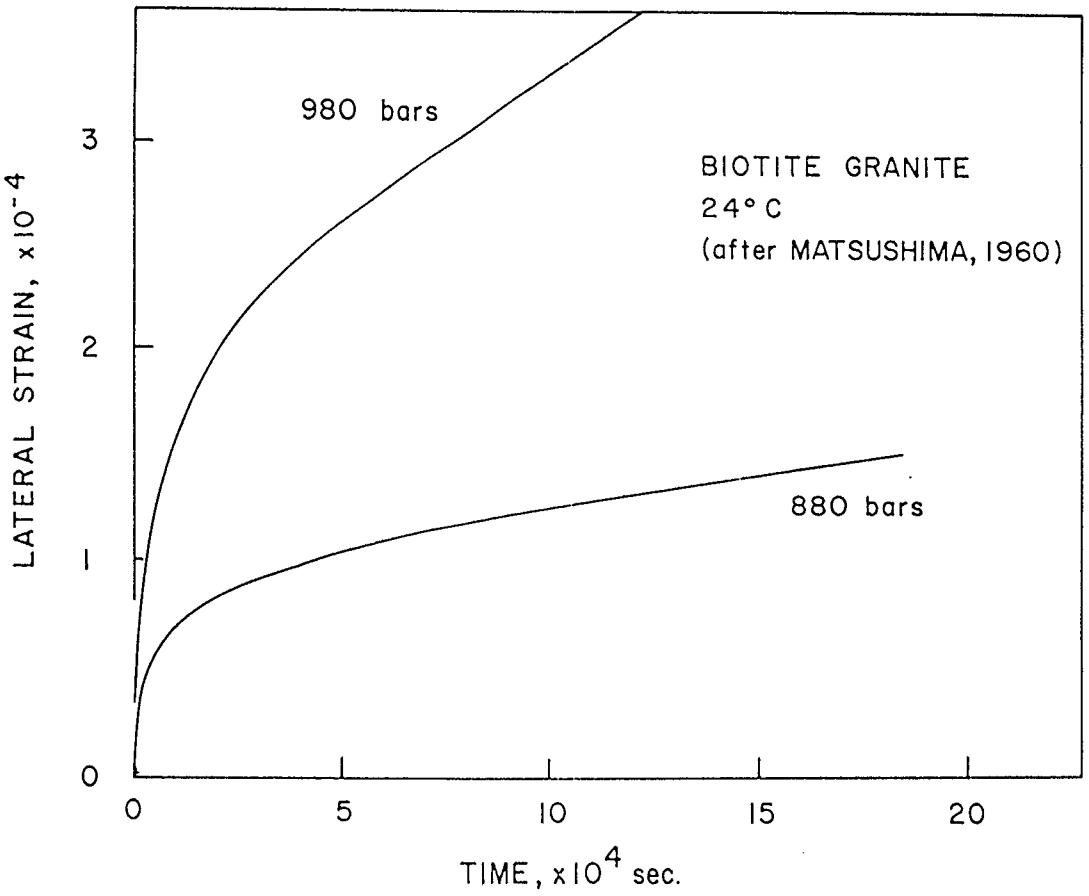

Figure 1: The change in lateral strain is plotted as a function of time for two creep experiments conducted on specimens of biotite granite (after Matsushima, 1960).

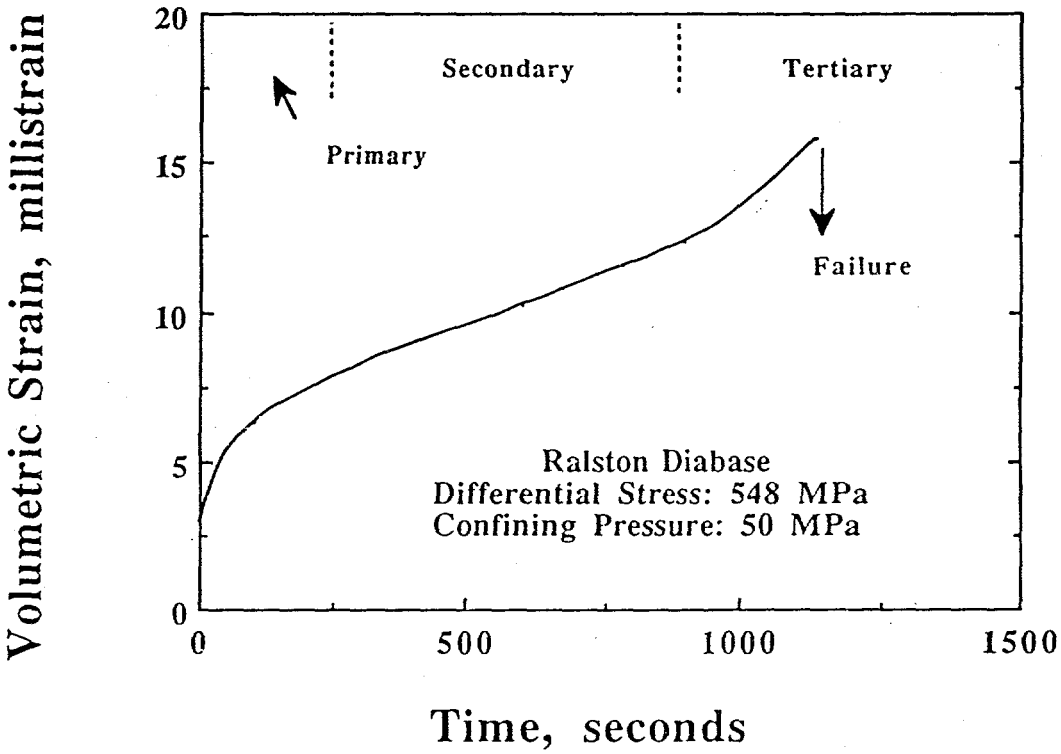

Figure 2: Volumetric strain is plotted as a function of time for a creep event on Ralston diabase (after Martin et al., 1978).

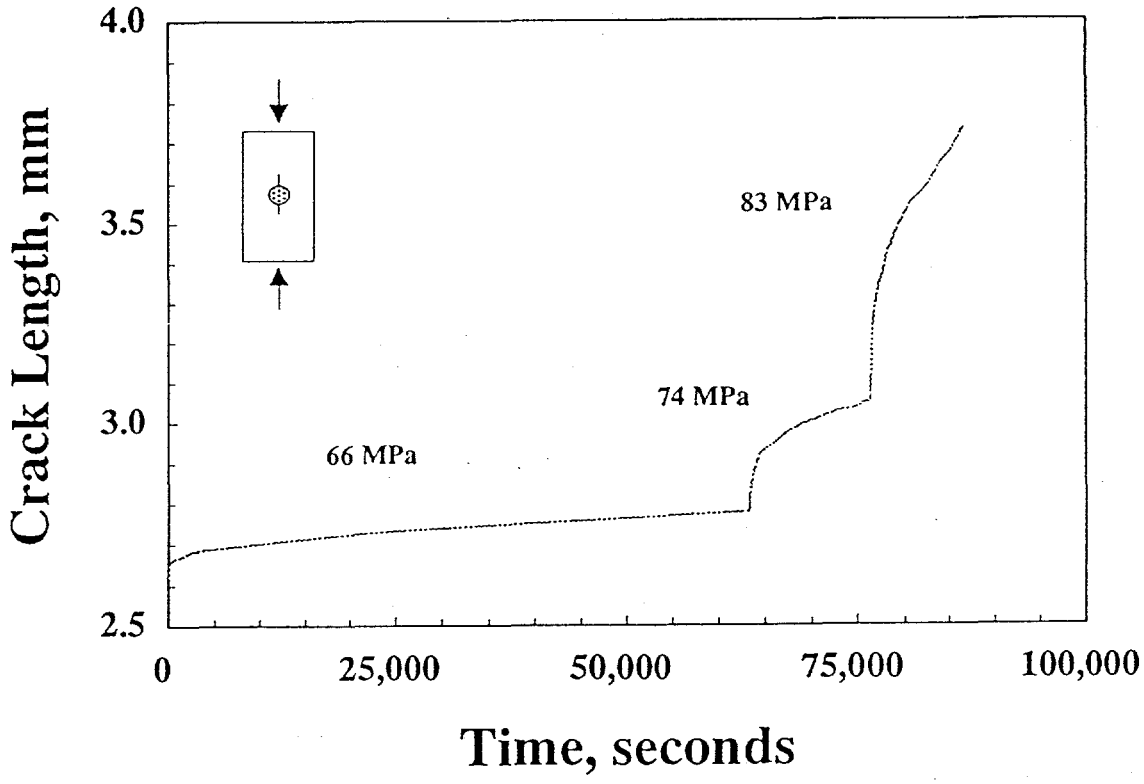

Figure 3: Crack length is shown as a function of time for an axial crack growth experiment in single crystal quartz. The experiment was conducted at a temperature of 241 ^{o}C and with a partial pressure of water of 4.5 x 10^{-2} kPa (after Martin, 1972).

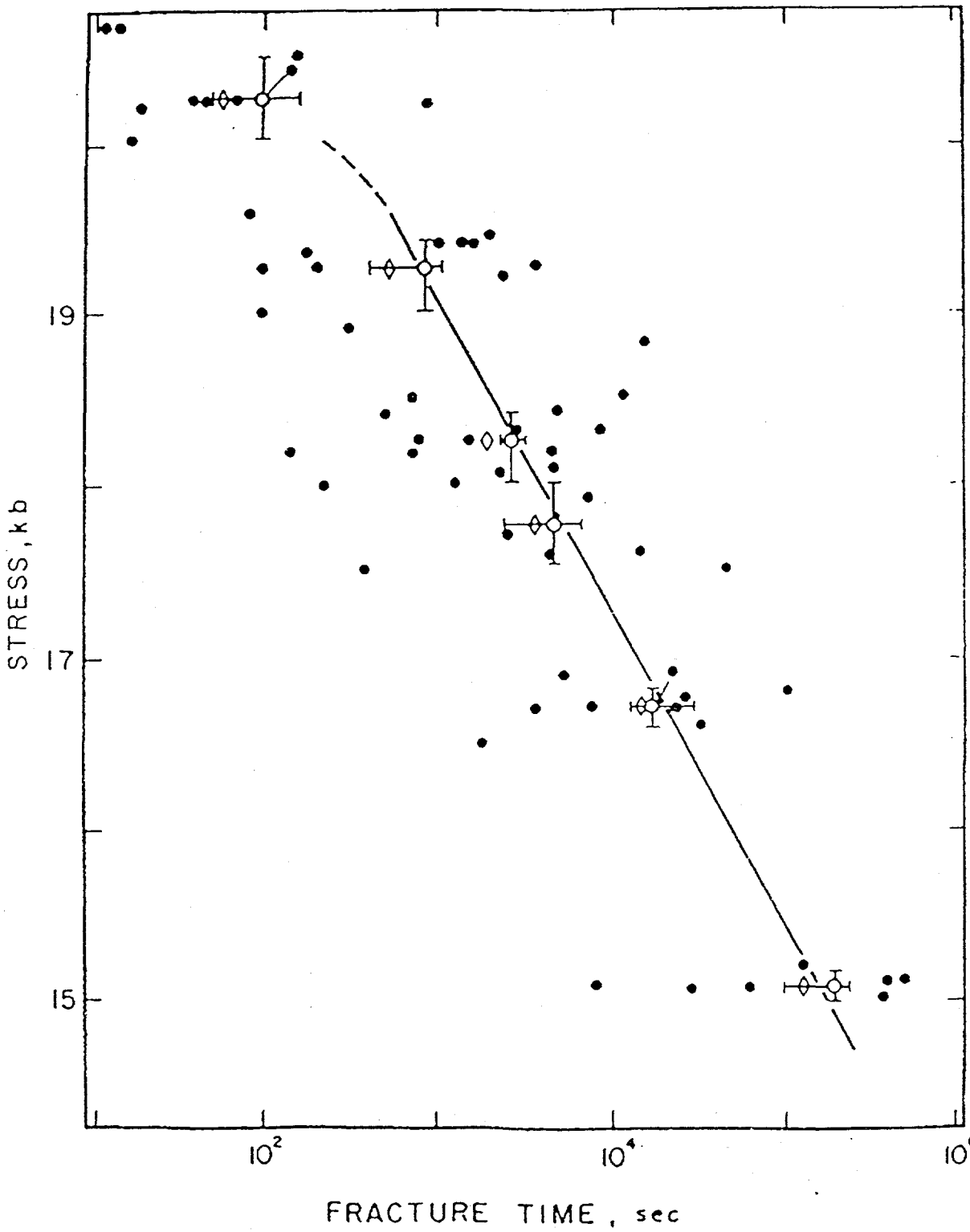

Figure 4: The failure stress of single crystal quartz is plotted as a function of time to failure. The tests were conducted at ambient temperature at a fixed partial pressure of water (after Scholz, 1972).

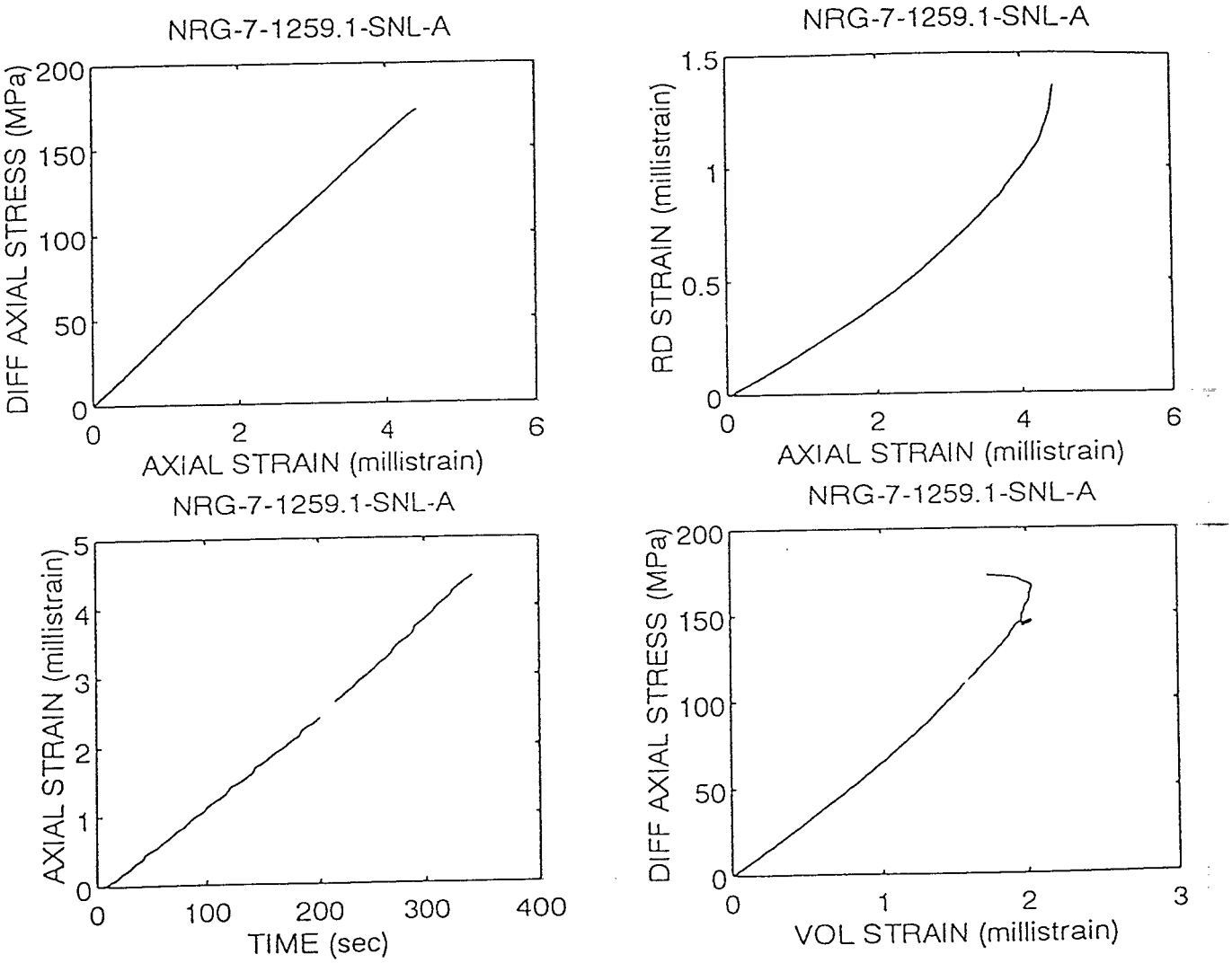

Figure 5: Data collected during an unconfined compression experiment on a specimen of Topopah Spring Member tuff (TSw2) recovered from borehole USW NRG-7/7A from a depth of 1259.1 feet. The experiment was conducted on a saturated specimen at a constant strain rate of 10^{-5} s^{-1}. The initial porosity of the specimen was 9.8%. Differential axial stress and radial strain is plotted as a function of axial strain in the upper portion of the figure. Axial strain is plotted as a function of time and differential axial stress as a function of volumetric strain in the lower portion of the figure.

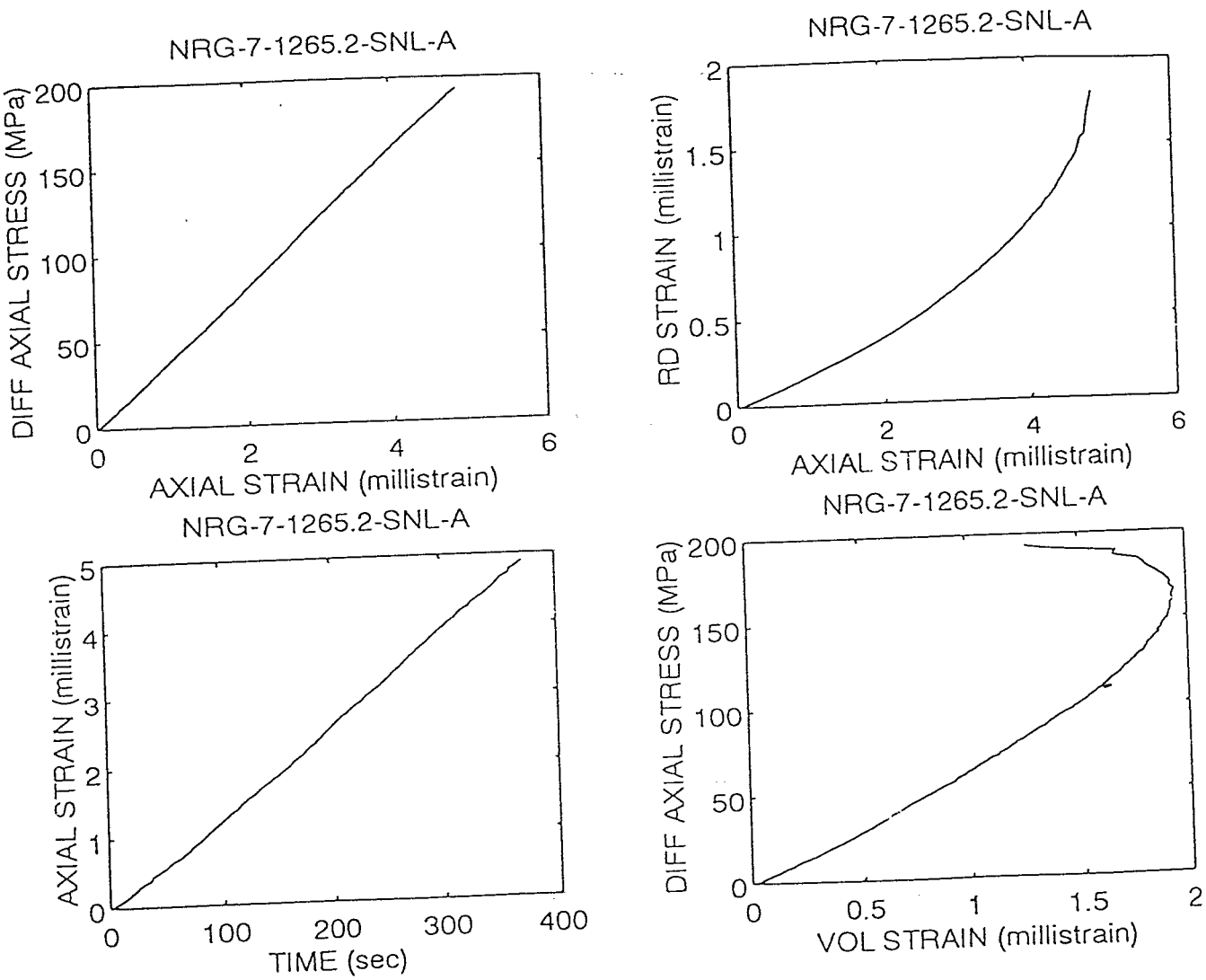

Figure 6: Data collected during an unconfined compression experiment on a specimen of Topopah Spring Member tuff (TSw2) recovered from borehole USW NRG-7/7A from a depth of 1265.2 feet. The experiment was conducted on a saturated specimen at a constant strain rate of 10^{-5} s^{-1}. The initial porosity of the specimen was 9.6%. Differential axial stress and radial strain is plotted as a function of axial strain in the upper portion of the figure. Axial strain is plotted as a function of time and differential axial stress as a function of volumetric strain in the lower portion of the figure.

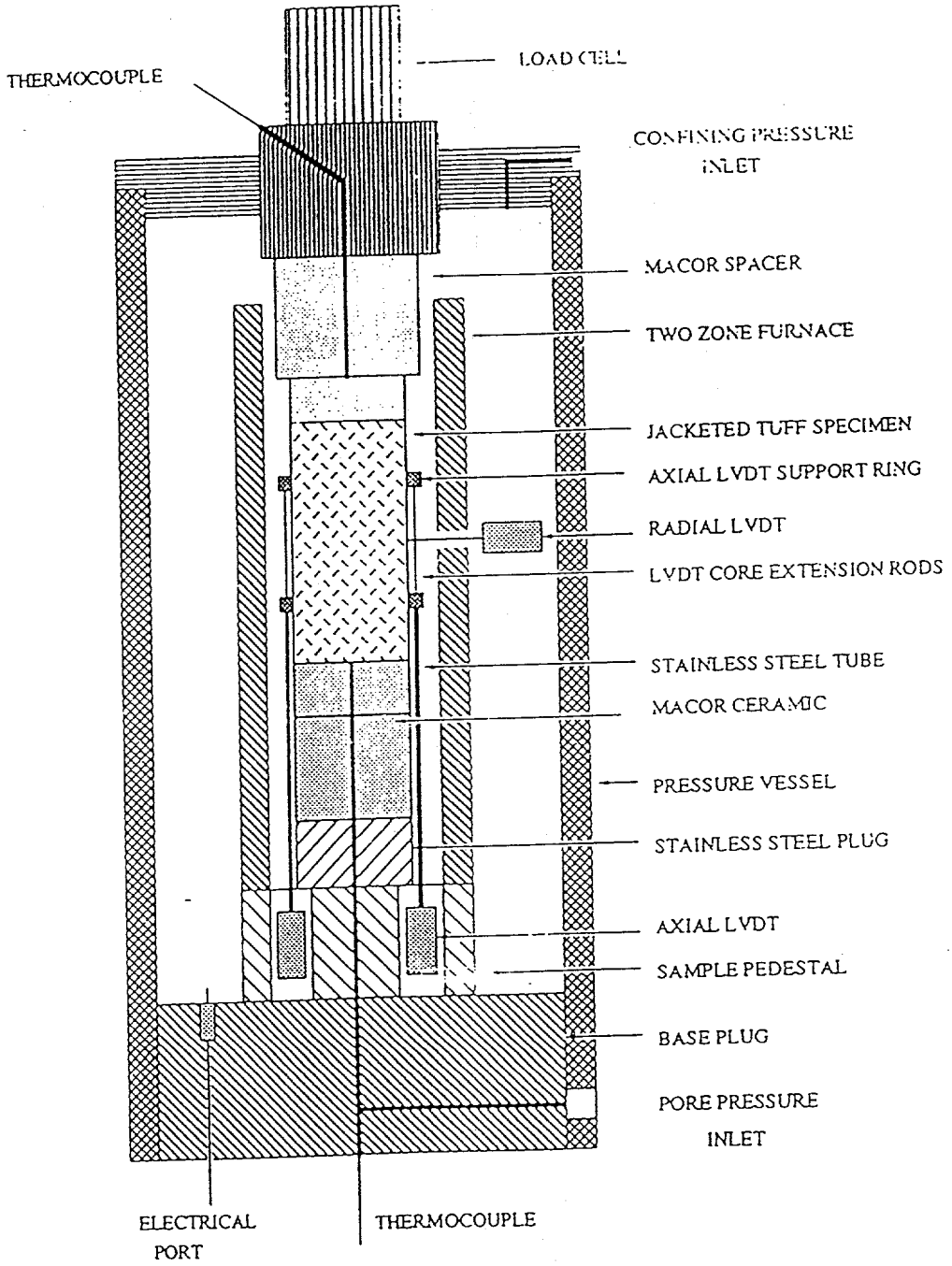

Figure 7: Schematic diagram of the pressure vessel, furnace assembly, and instrumentation used for the constant stress creep tests at 250 °C.

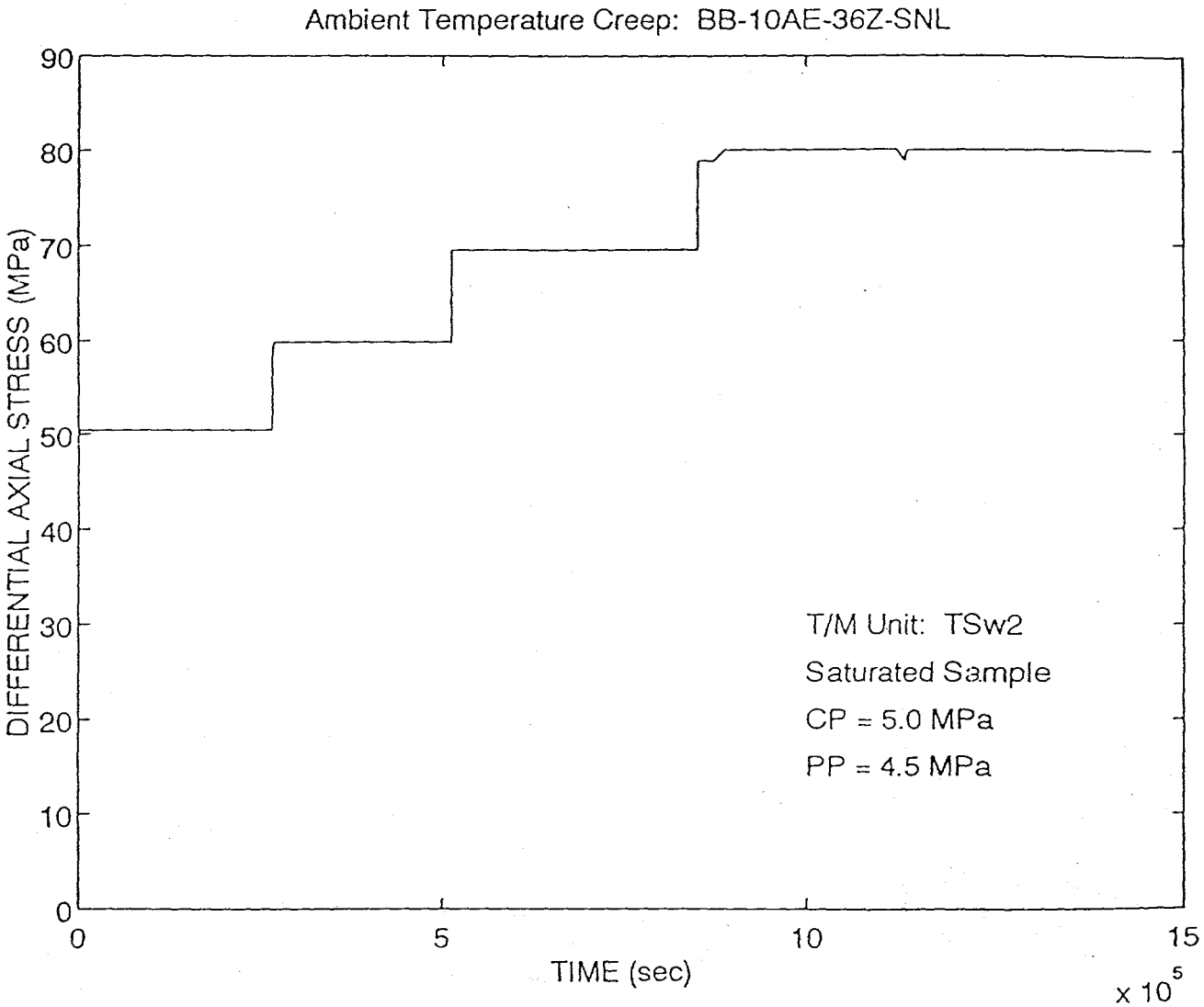

Figure 8a: The loading history for the creep experiment conducted at ambient temperature on specimen BB-10AE-36Z-SNL. Differential axial stress is plotted as a function of time. The experiment was conducted at a confining pressure of 5.0 MPa and a pore pressure of 4.5 MPa.

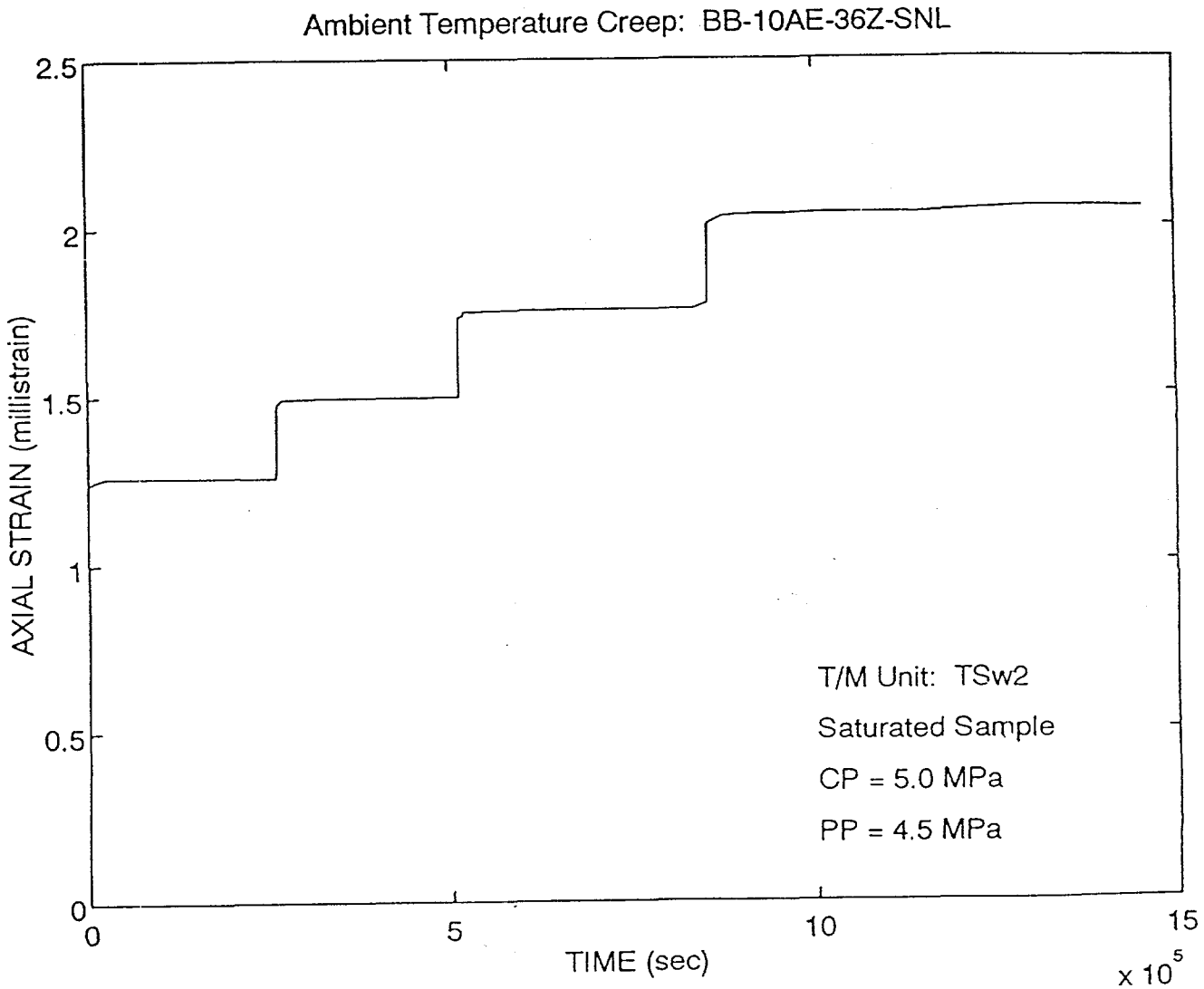

Figure 8b: Axial strain is plotted as a function of time for the ambient temperature creep experiment on specimen BB-10AE-36Z-SNL. The experiment was conducted at a confining pressure of 5.0 MPa and a pore pressure of 4.5 MPa.

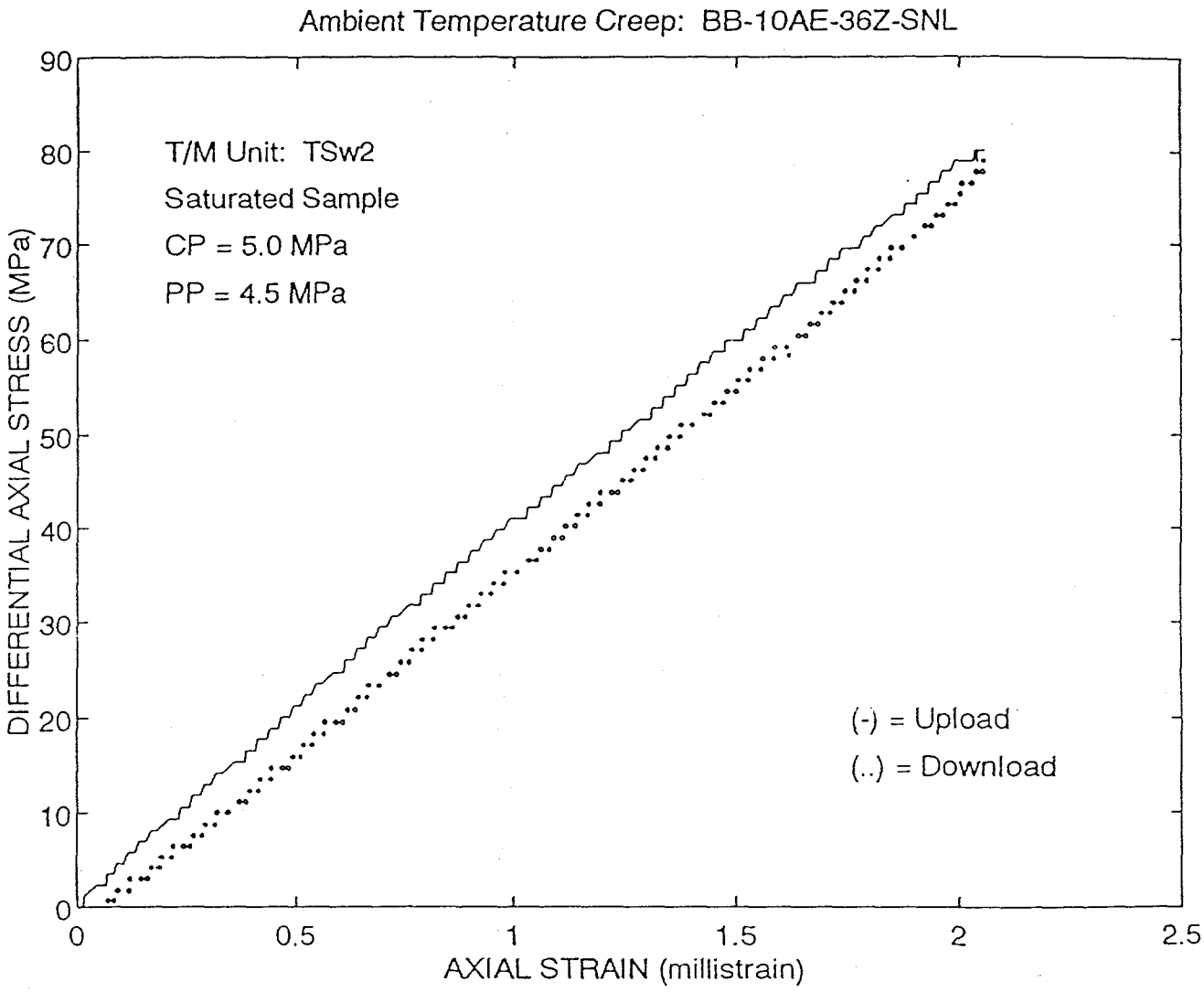

Figure 8c: A stress-strain curve was prepared from the ambient temperature creep data on specimen BB-10AE-36Z-SNL. Differential axial stress is plotted as a function of axial strain. The experiment was conducted at a confining pressure of 5.0 MPa and a pore pressure of 4.5 MPa.

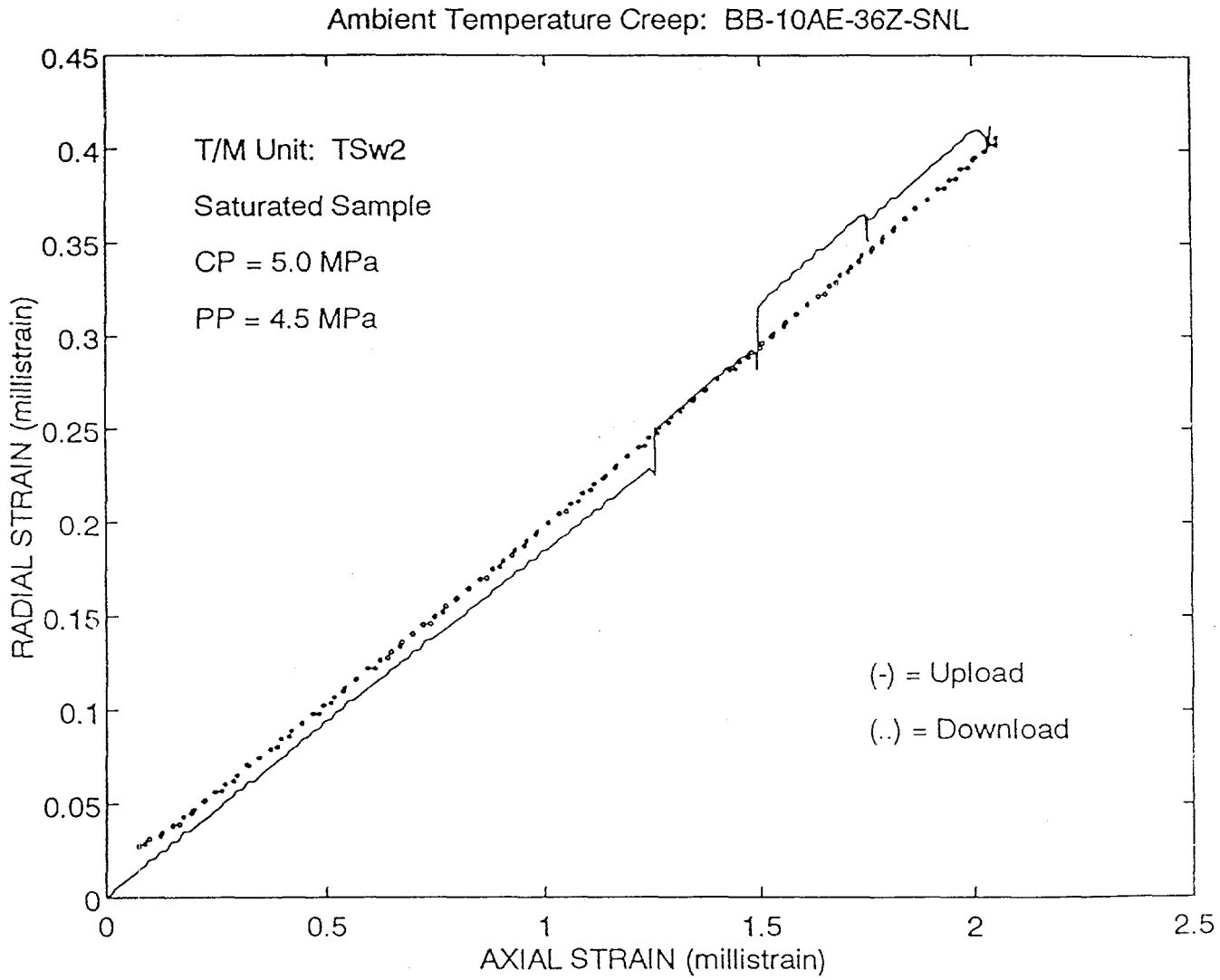

Figure 8d: Radial strain is plotted as a function of axial strain for the data collected during the ambient temperature creep experiment on specimen BB-10AE-36Z-SNL. The experiment was conducted at a confining pressure of 5.0 MPa and a pore pressure of 4.5 MPa.

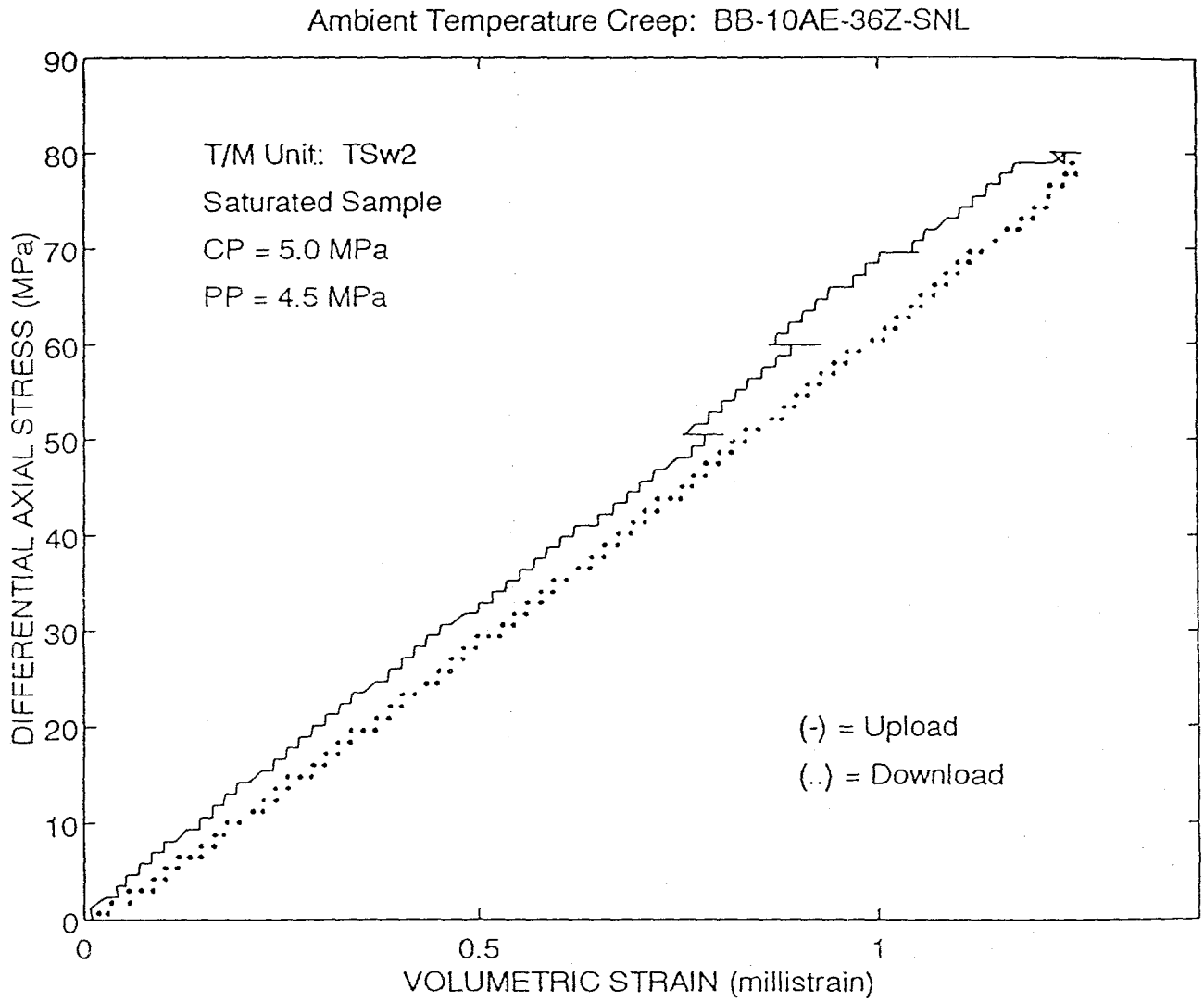

Figure 8e: Differential axial stress is plotted as a function of volumetric strain for the ambient temperature creep data collected on specimen BB-10AE-36Z-SNL. The experiment was conducted at a confining pressure of 5.0 MPa and a pore pressure of 4.5 MPa.

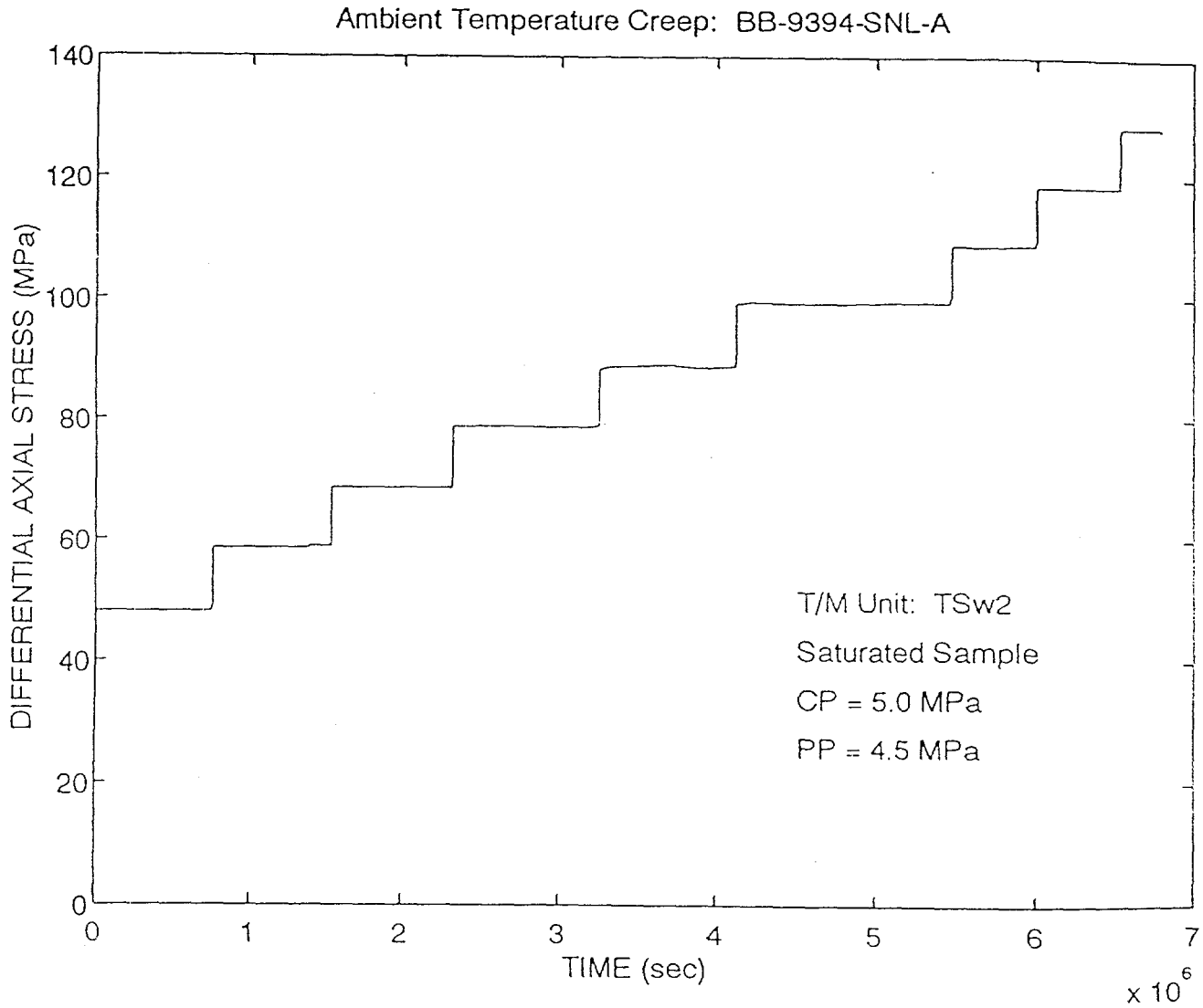

Figure 9a: The loading history for the ambient temperature creep experiment on specimen BB-9394-SNL-A. Differential axial stress is plotted as a function of time. The experiment was conducted at a confining pressure of 5.0 MPa and a pore pressure of 4.5 MPa.

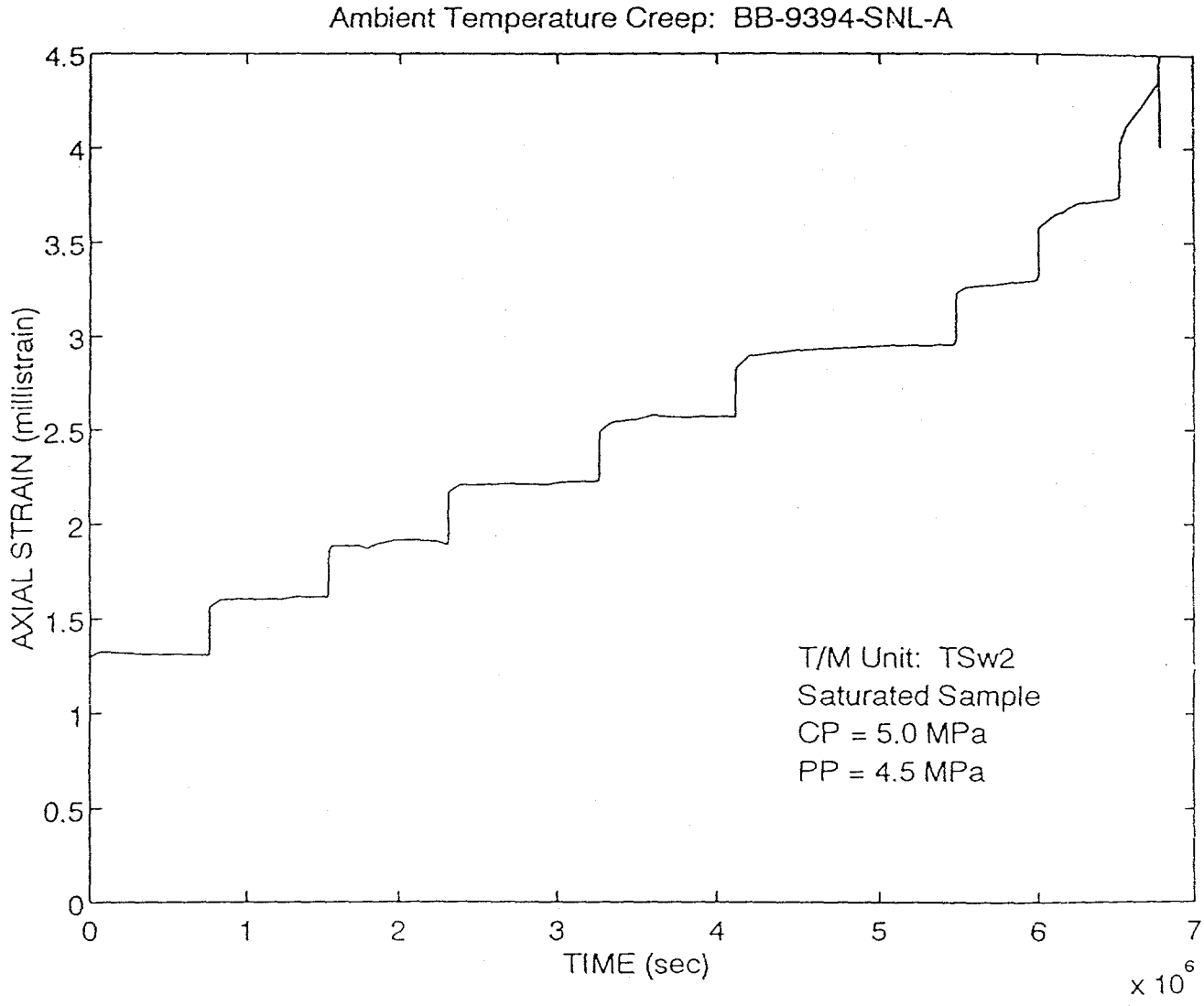

Figure 9b: Axial strain data collected during the ambient temperature creep experiment on specimen BB-9394-SNL-A is plotted as a function of time. The experiment was conducted at a confining pressure of 5.0 MPa and a pore pressure of 4.5 MPa.

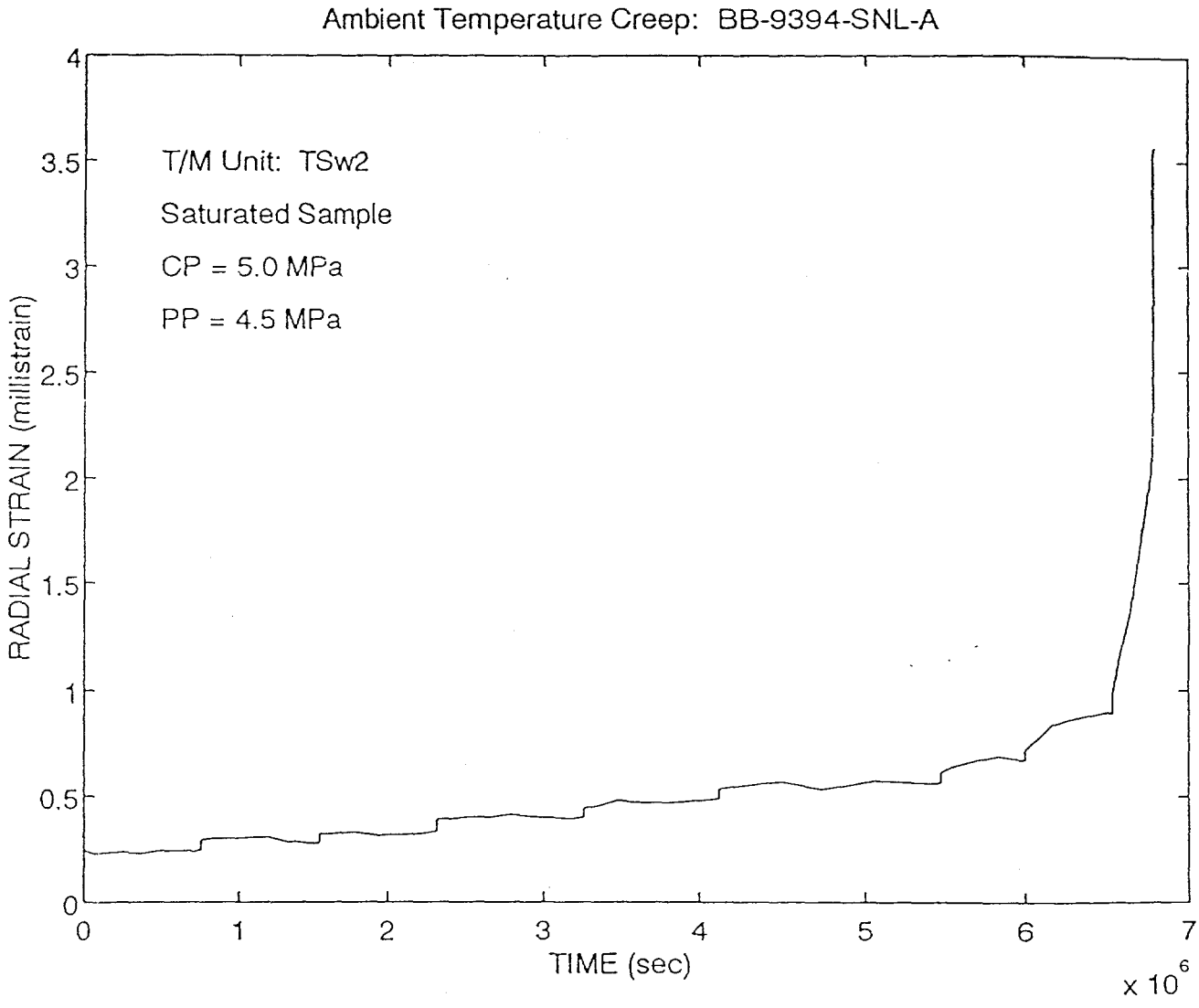

Figure 9c: Radial strain is plotted as a function of time for the ambient temperature creep experiment on specimen BB-9394-SNL-A. The experiment was conducted at a confining pressure of 5.0 MPa and a pore pressure of 4.5 MPa.

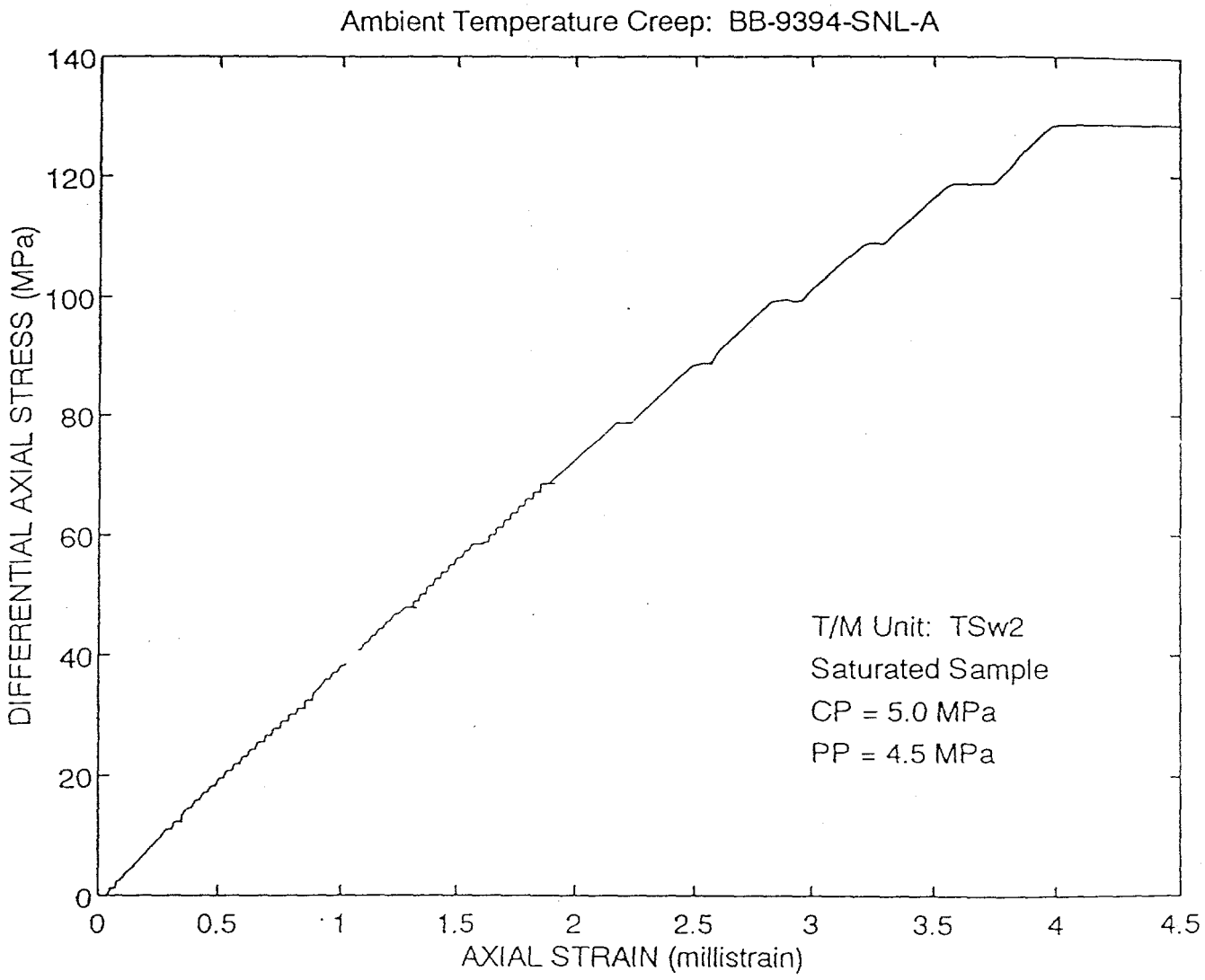

Figure 9d: The data obtained on the ambient temperature creep experiment on BB-9394-SNL-A is presented in a conventional stress-strain curve. The differential axial stress is plotted as a function of axial strain. The experiment was conducted at a confining pressure of 5.0 MPa and a pore pressure of 4.5 MPa.

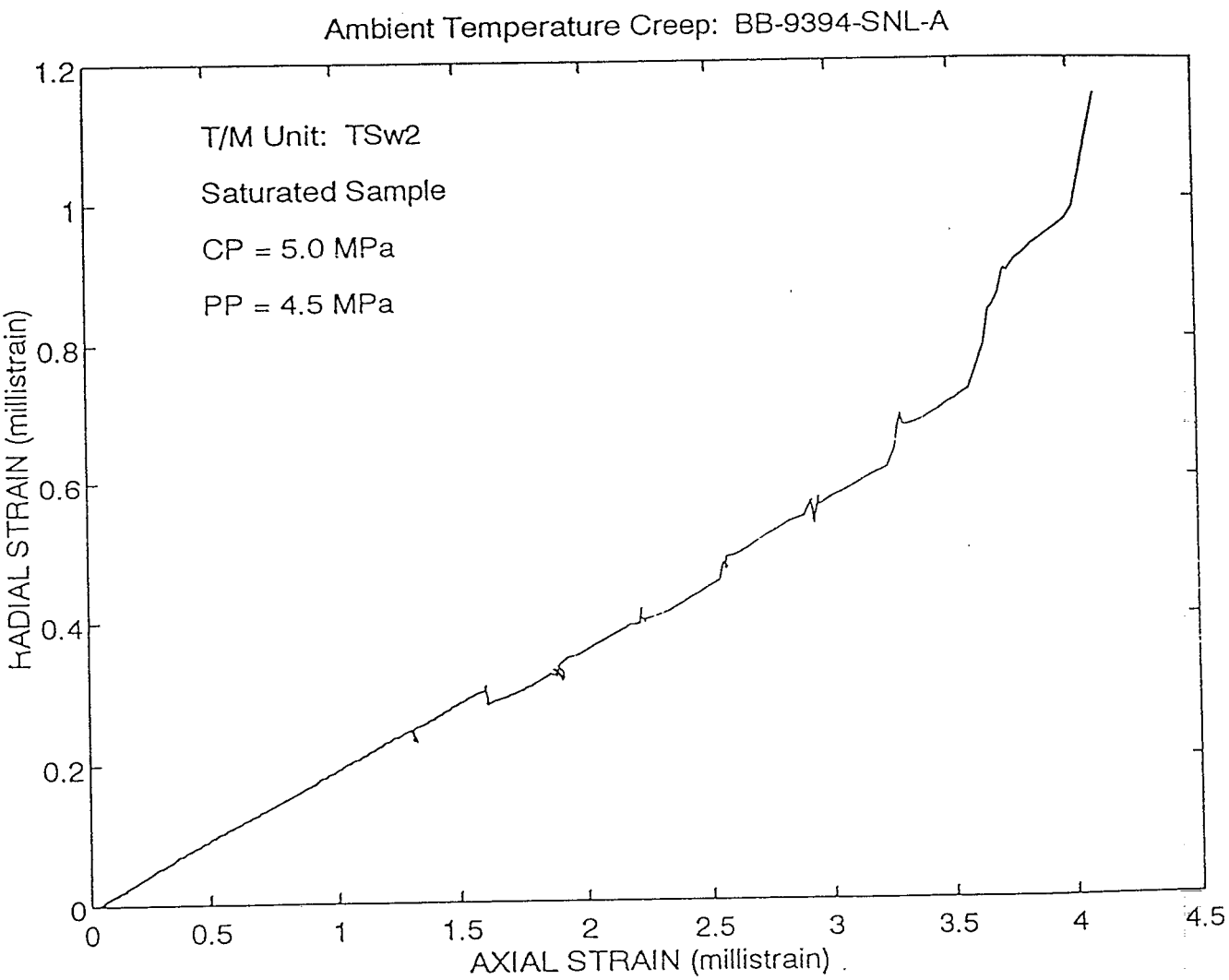

Figure 9e: Radial strain is plotted as a function of axial strain for the data collected on the ambient temperature creep experiment on specimen BB-9394-SNL-A. The experiment was conducted at a confining pressure of 5.0 MPa and a pore pressure of 4.5 MPa.

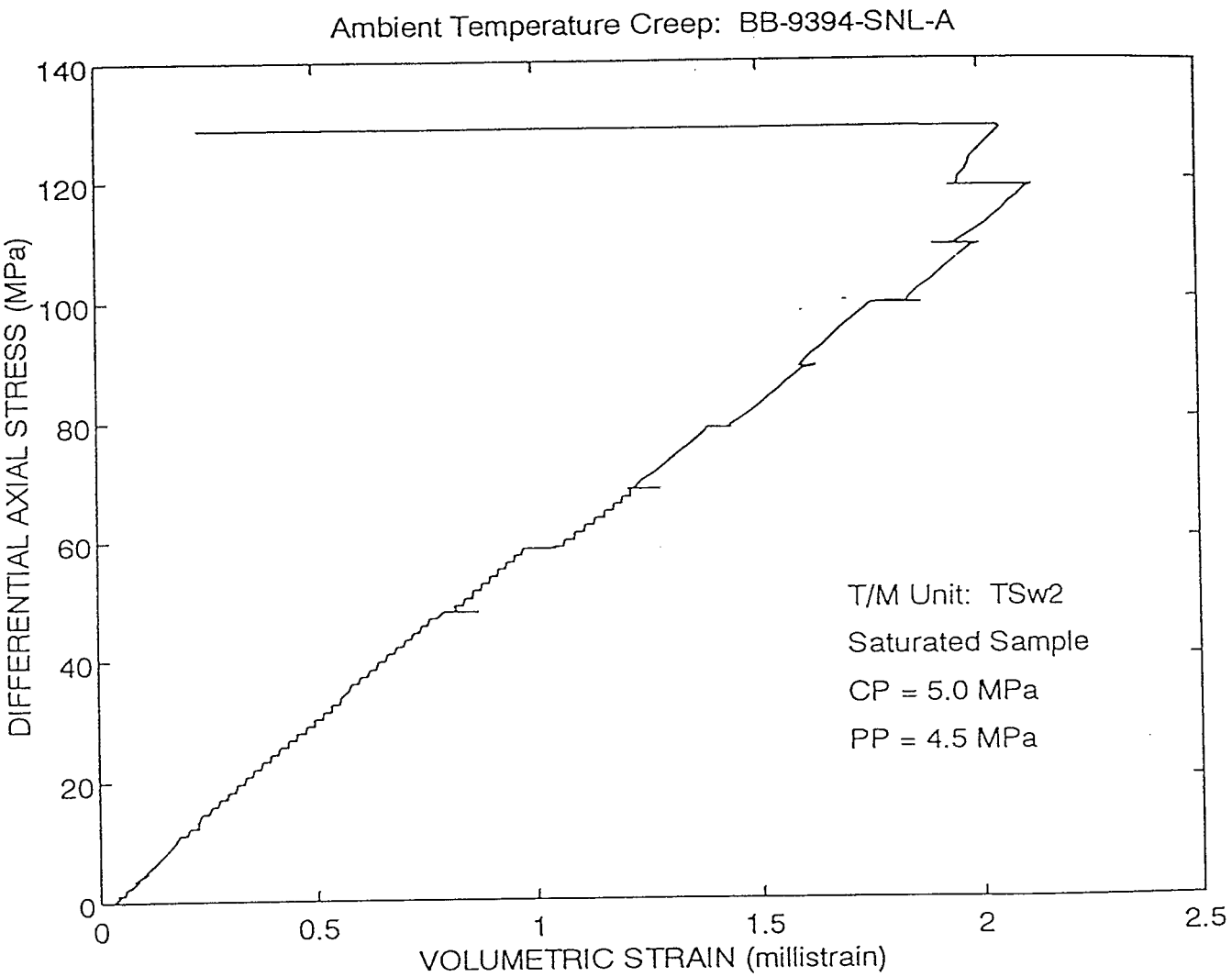

Figure 9f: Differential axial stress is plotted as a function of volumetric strain for the ambient temperature creep data collected on specimen BB-9394-SNL-A. The experiment was conducted at a confining pressure of 5.0 MPa and a pore pressure of 4.5 MPa.

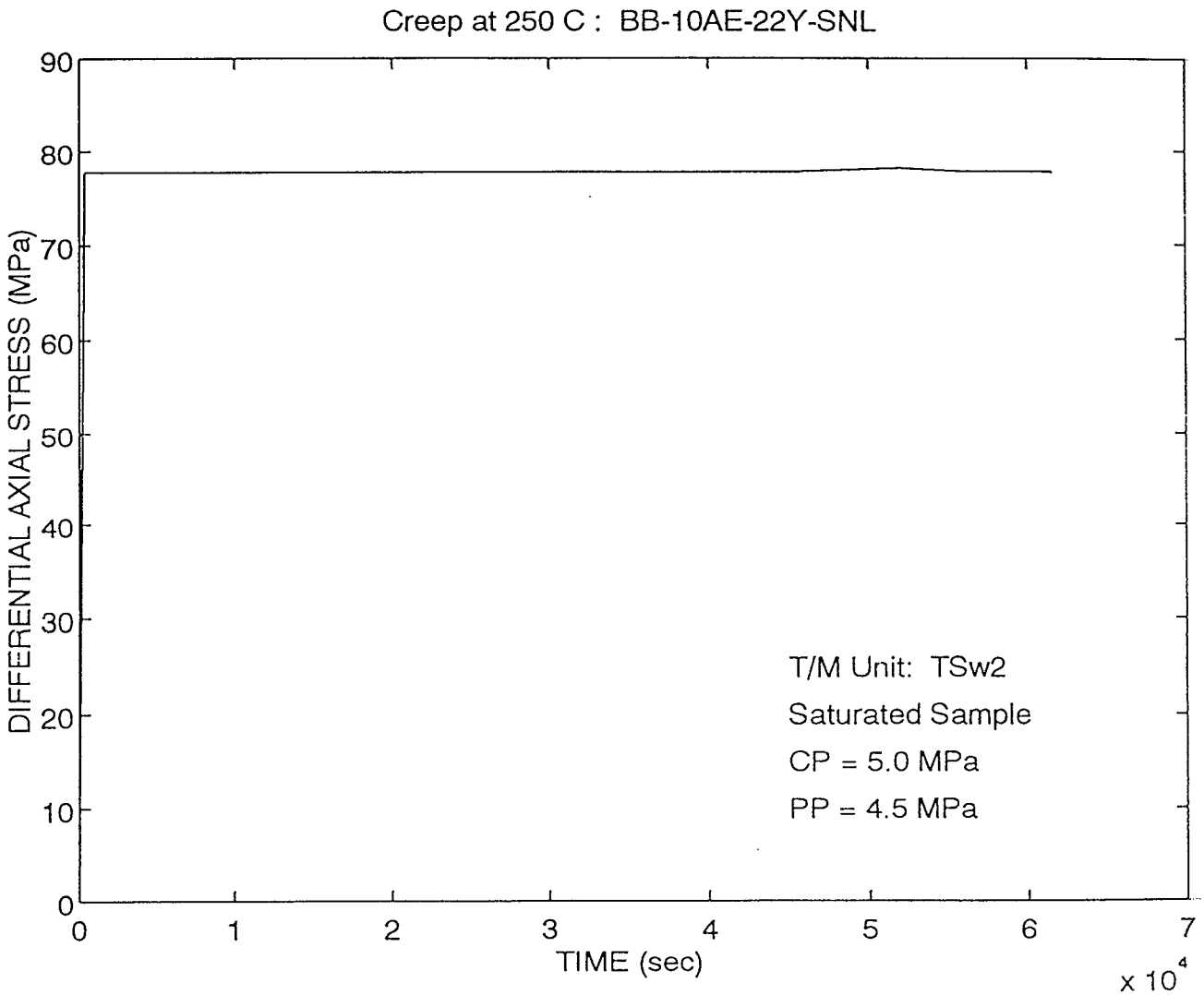

Figure 10a: The loading history for a creep experiment on specimen BB-10AE-22Y-SNL at a temperature of 250 °C is shown. Differential axial stress is plotted as a function of time. The experiment was conducted at a confining pressure of 5.0 MPa and a pore pressure of 4.5 MPa.

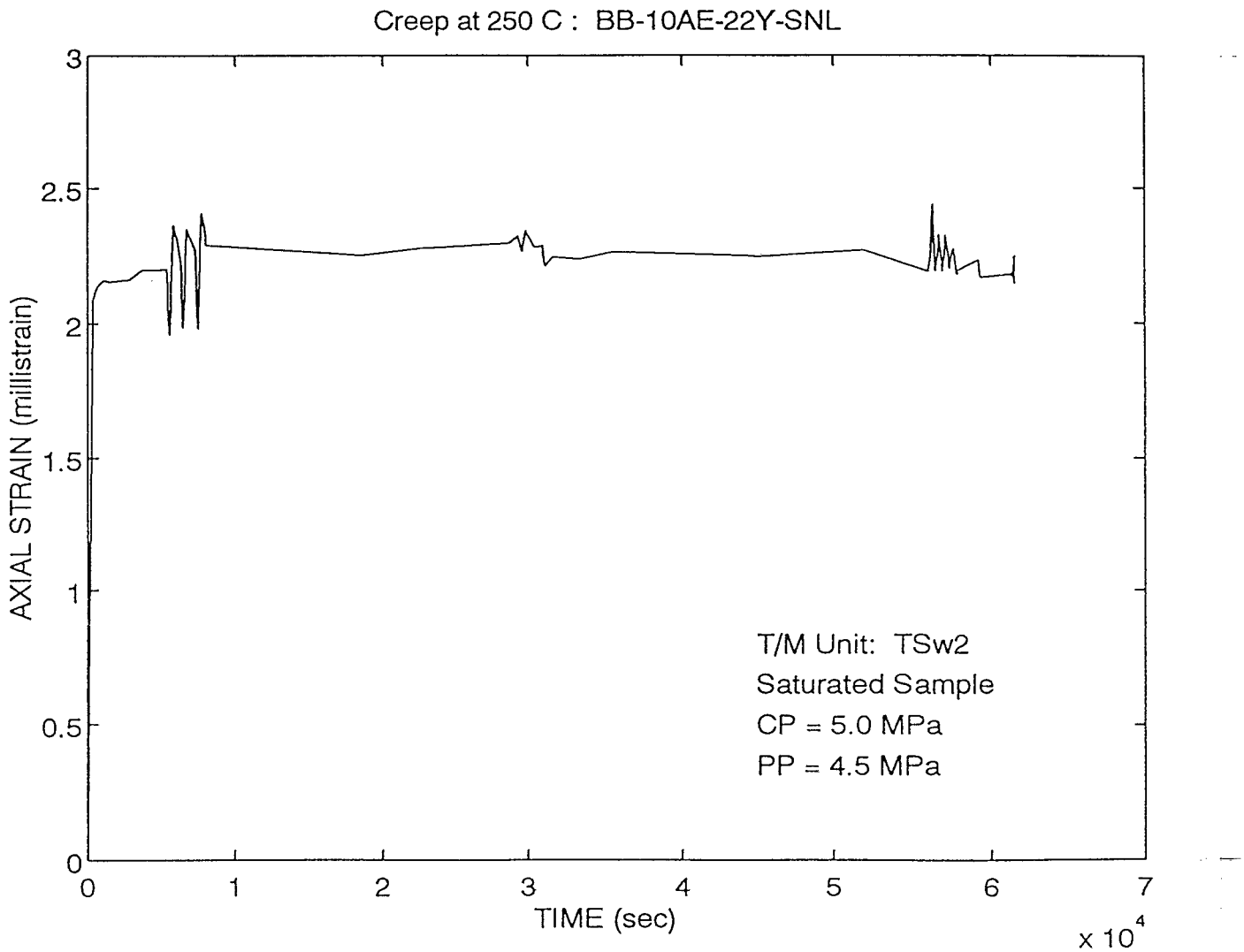

Figure 10b: Axial strain is plotted as a function of time for the high temperature creep experiment on specimen BB-10AE-22Y-SNL. The differential axial stress was held constant at 77.7 MPa. The experiment was conducted at a confining pressure of 5.0 MPa and a pore pressure of 4.5 MPa.

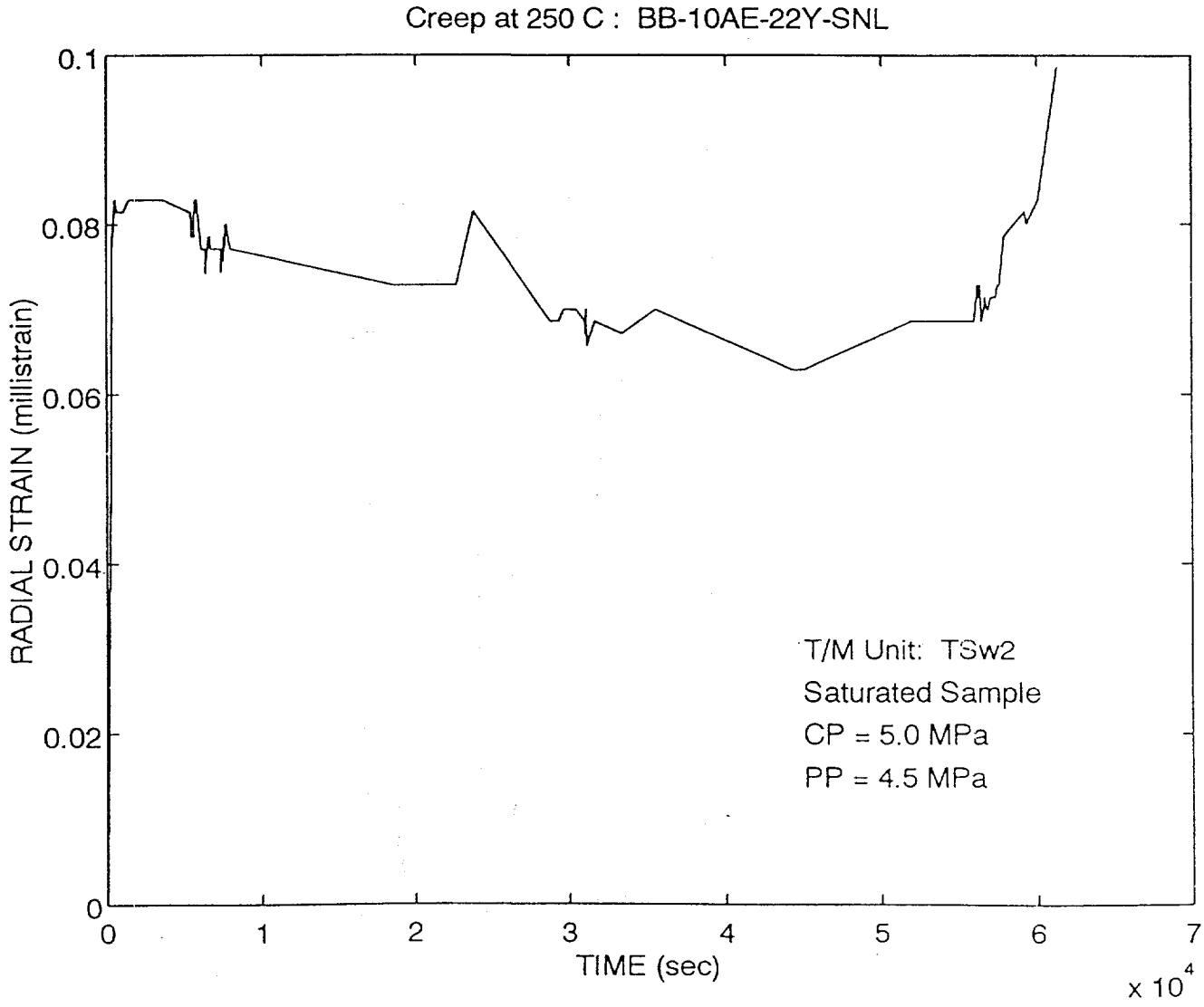

Figure 10c: Radial strain is plotted as a function of time for the creep experiment conducted at 250 °C on specimen BB-10AE-22Y-SNL. The experiment was conducted at a confining pressure of 5.0 MPa and a pore pressure of 4.5 MPa.

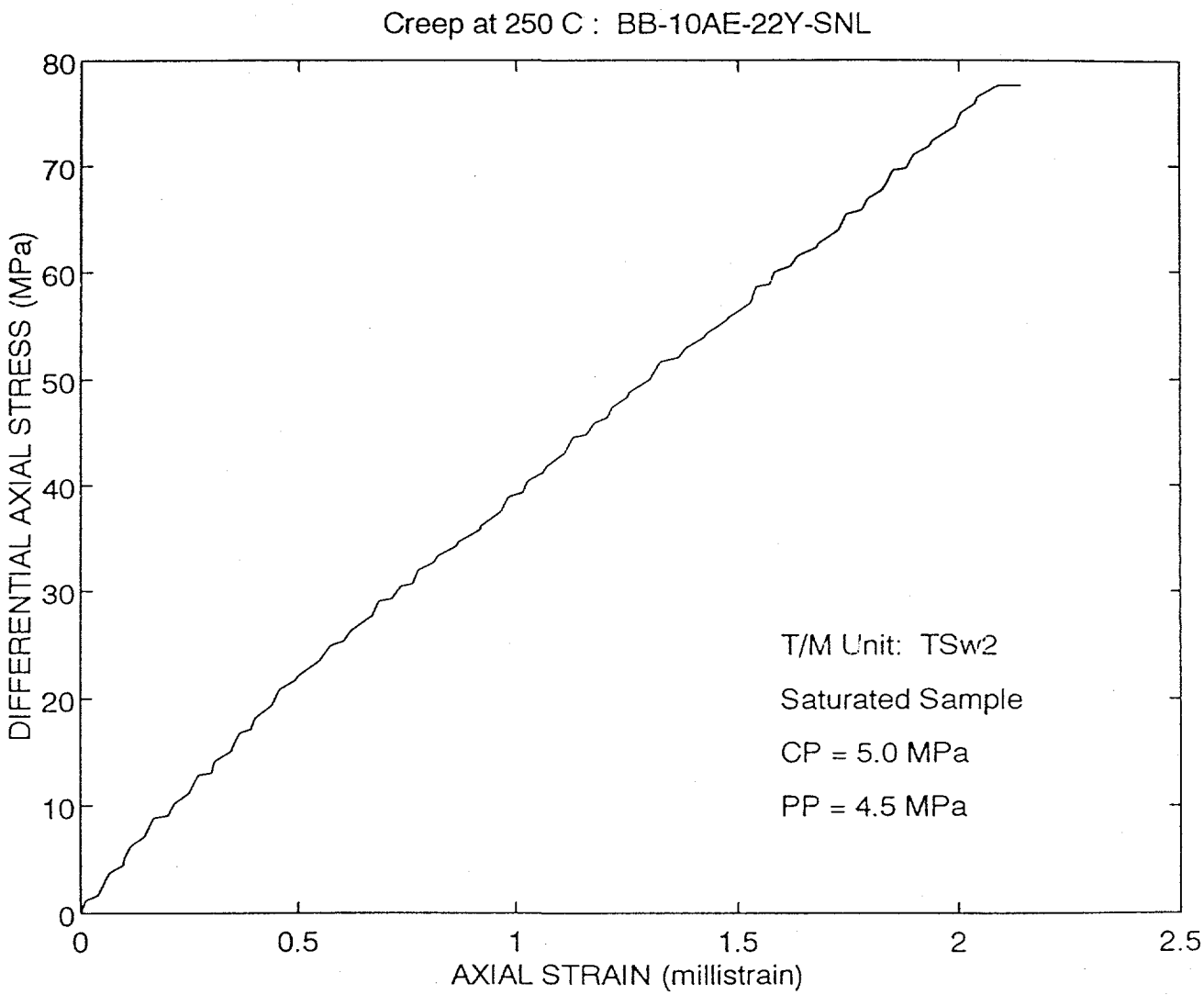

Figure 10d: Differential axial stress is plotted as a function of axial strain for the high temperature creep experiment conducted on specimen BB-10AE-22Y-SNL. The data include those collected from the constant stress rate loading as well as the creep event. The experiment was conducted at a confining pressure of 5.0 MPa and a pore pressure of 4.5 MPa.

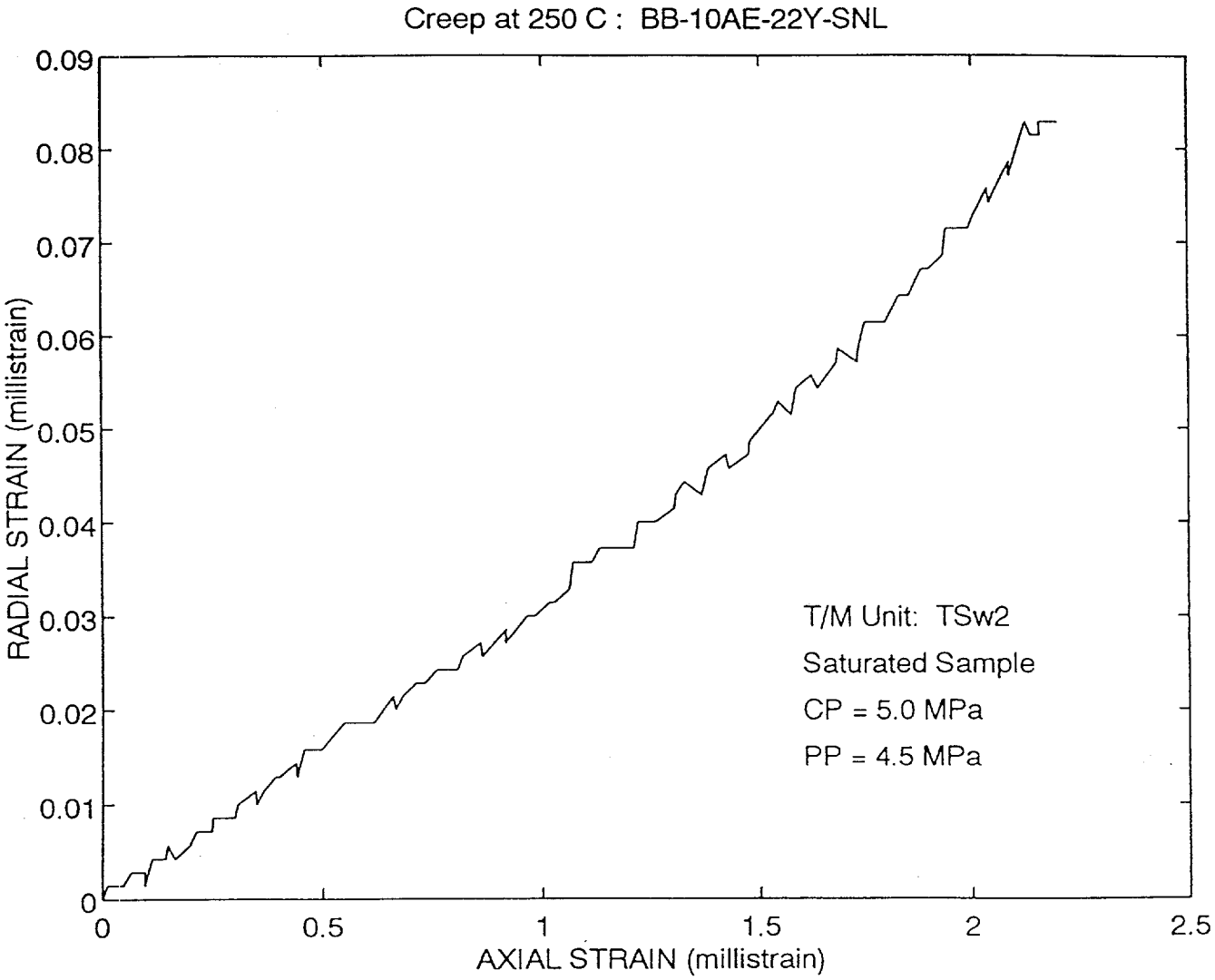

Figure 10e: Radial strain is plotted as a function of axial strain for the high temperature creep experiment conducted on specimen BB-10AE-22Y-SNL. The data include those collected during the constant stress rate loading of the specimen to a differential axial stress of 77.7 MPa. The experiment was conducted at a confining pressure of 5.0 MPa and a pore pressure of 4.5 MPa.

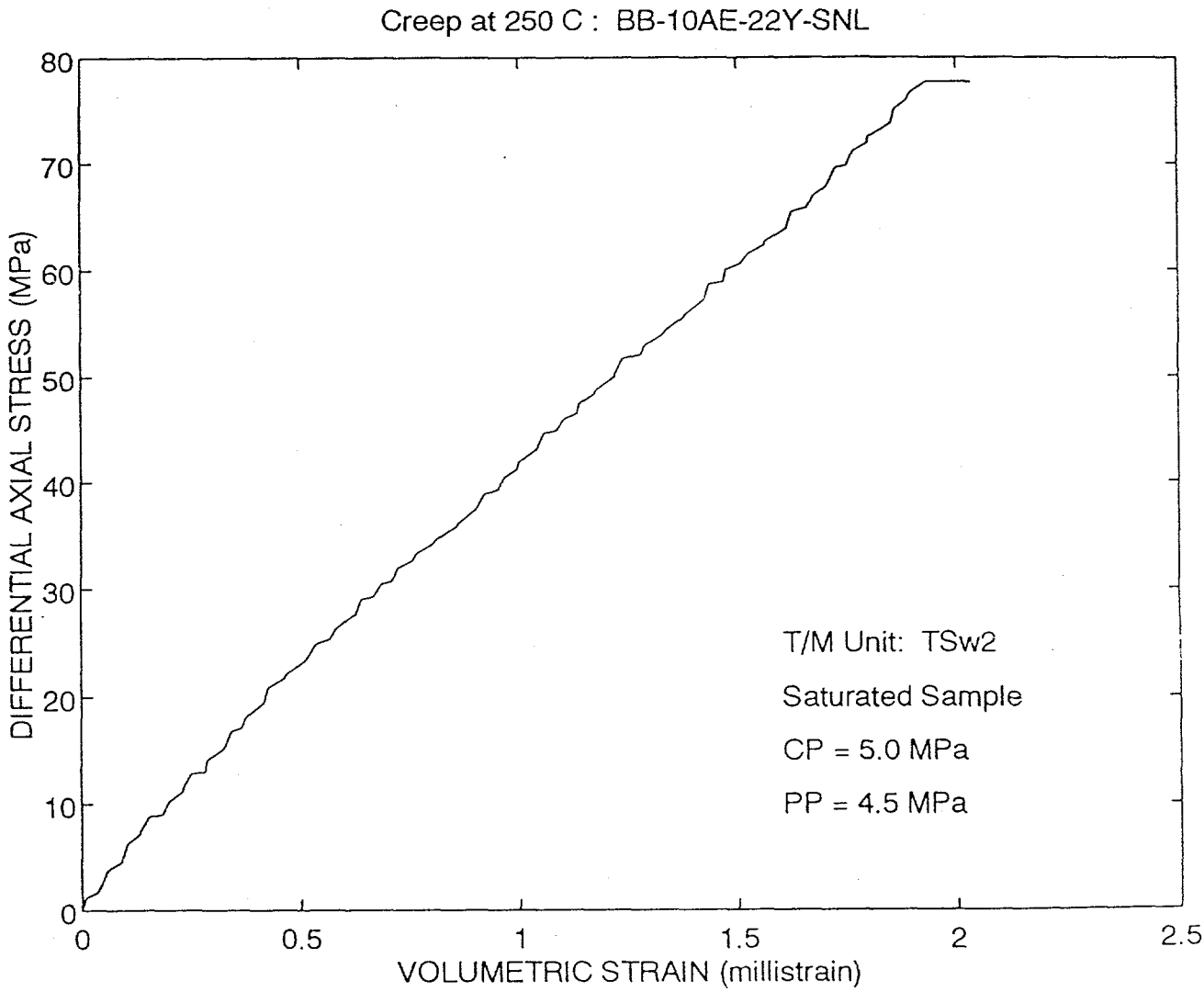

Figure 10f: Differential axial stress is plotted as a function of volumetric strain for the high temperature creep experiments conducted on specimen BB-10AE-22Y-SNL. The experiment was conducted at a confining pressure of 5.0 MPa and a pore pressure of 4.5 MPa.

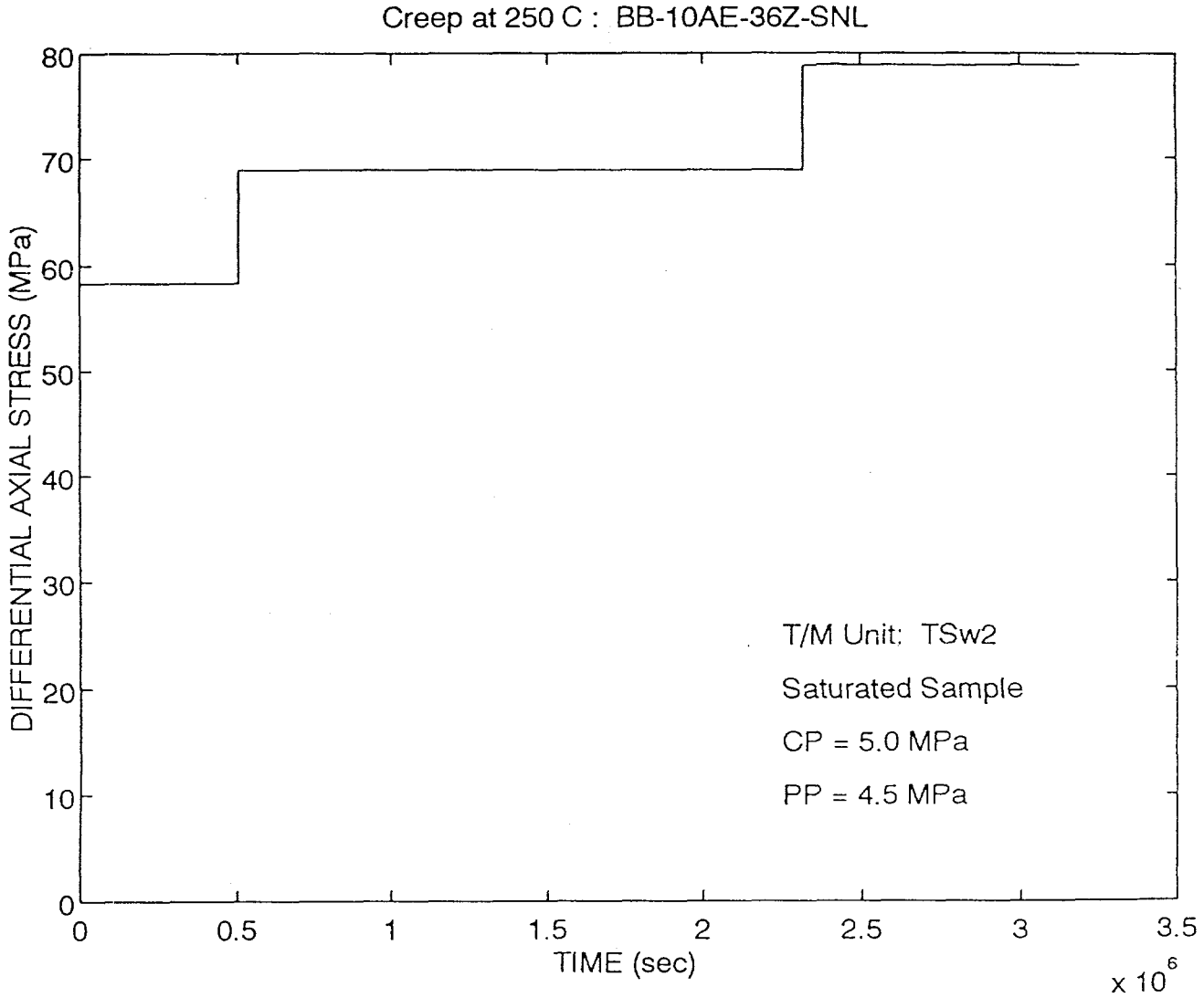

Figure 11a: The loading history is shown for the creep experiment at 250 °C on specimen BB-10AE-36Z-SNL. Differential axial stress is plotted as a function of time. The experiment was conducted at a confining pressure of 5.0 MPa and a pore pressure of 4.5 MPa.

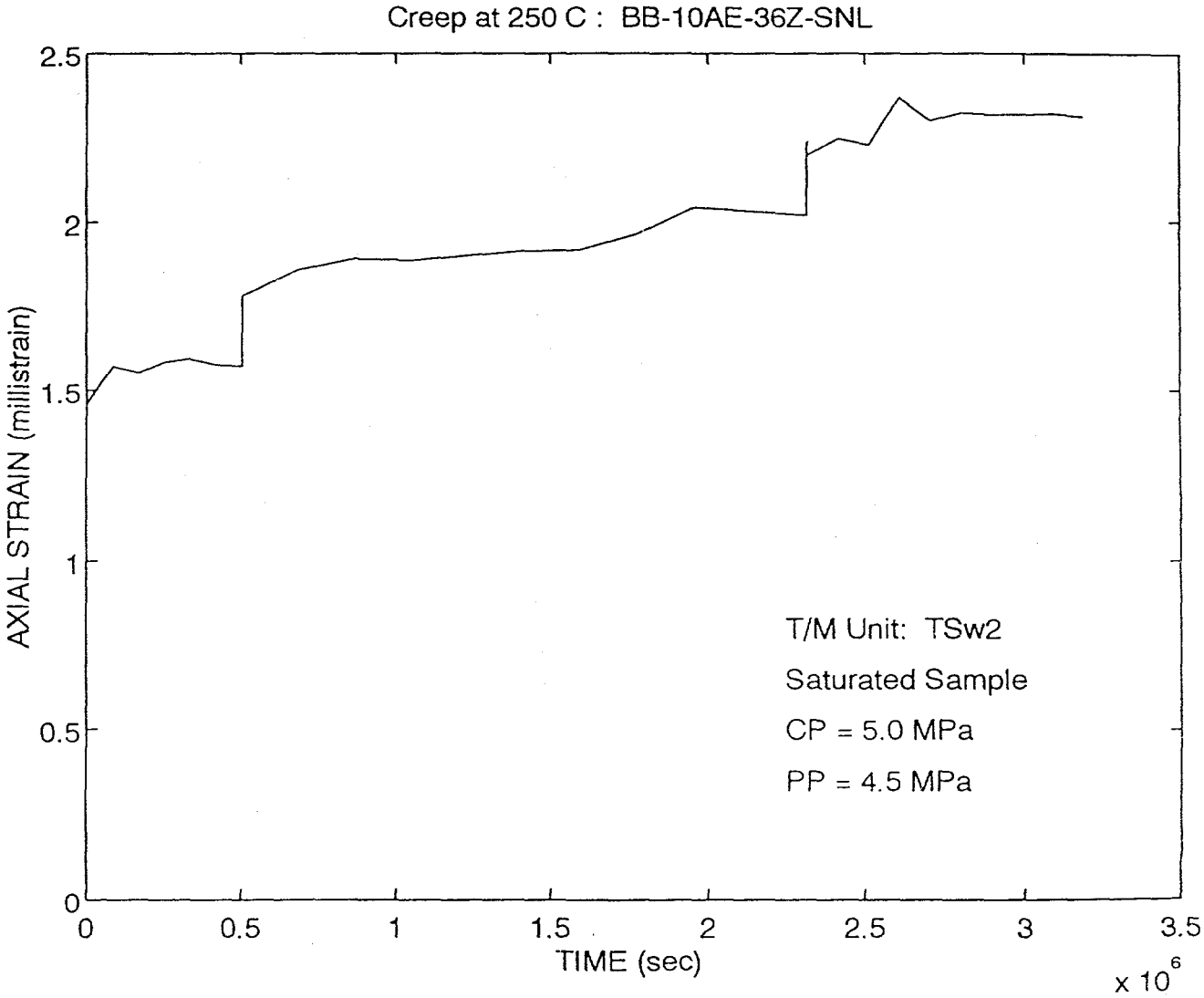

Figure 11b: Axial strain is plotted as a function of time for the creep experiment conducted at 250 °C on specimen BB-10AE-36Z-SNL. The experiment was conducted at a confining pressure of 5.0 MPa and a pore pressure of 4.5 MPa.

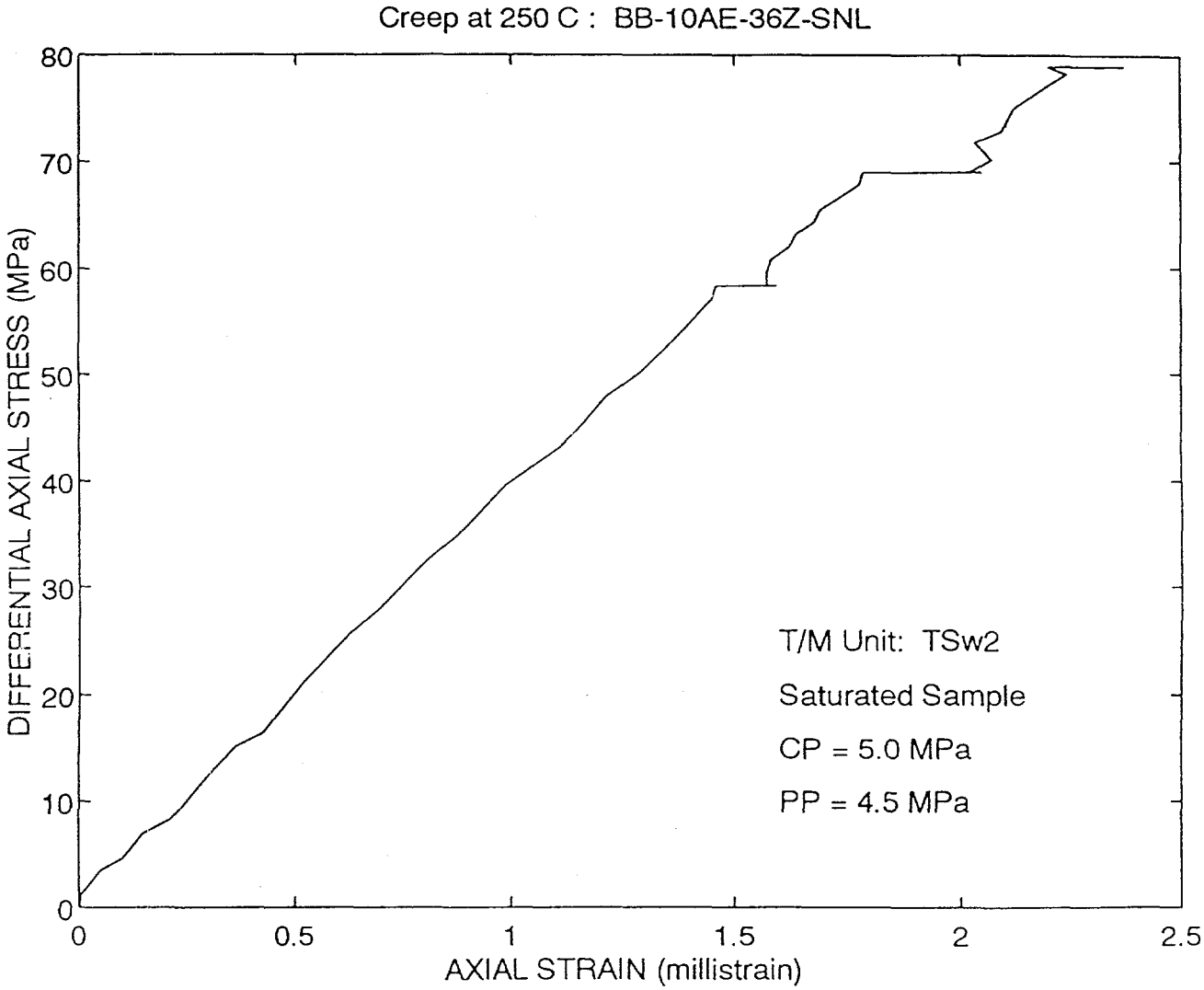

Figure 11c: Differential axial stress is plotted as a function of axial strain for the data collected during the high temperature creep experiment on specimen BB-10AE-36Z-SNL. The experiment was conducted at 250 ^{o}C with a confining pressure of 5.0 MPa and a pore pressure of 4.5 MPa.

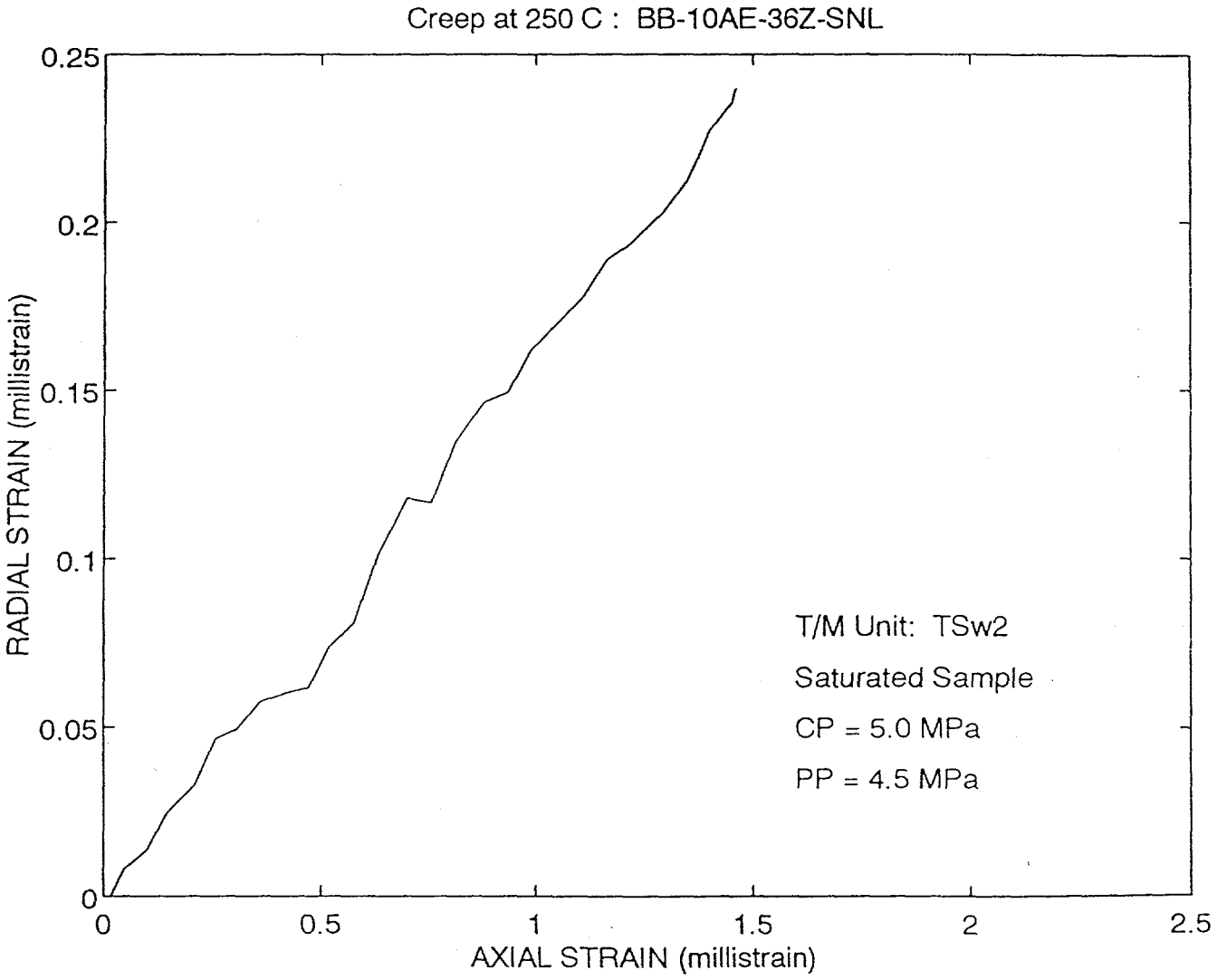

Figure 11d: Radial strain is plotted as a function of axial strain for the data collected during the creep experiment conducted on specimen BB-10AE-36Z-SNL. The experiment was conducted at 250 °C with a confining pressure of 5.0 MPa and a pore pressure of 4.5 MPa.

YUCCA MOUNTAIN SITE CHARACTERIZATION PROJECT

UC814 - DISTRIBUTION LIST

1 D. A. Dreyfus (RW-1)
Director
OCRWM
US Department of Energy
1000 Independence Avenue SW
Washington, DC 20585

1 L. H. Barrett (RW-2)
Acting Deputy Director
OCRWM
US Department of Energy
1000 Independence Avenue SW
Washington, DC 20585

1 J. D. Saltzman (RW-4)
Office of Strategic Planning and
International Programs
OCRWM
US Department of Energy
1000 Independence Avenue SW
Washington, DC 20585

1 J. D. Saltzman (RW-5)
Office of External Relations
OCRWM
US Department of Energy
1000 Independence Avenue SW
Washington, DC 20585

1 Samuel Rousso (RW-10)
Office of Program and Resource Mgt.
OCRWM
US Department of Energy
1000 Independence Avenue SW
Washington, DC 20585

1 J. C. Bresee (RW-10)
OCRWM
US Department of Energy
1000 Independence Avenue SW
Washington, DC 20585

1 S. Rousso (RW-50)
Office of Contract Business
Management
OCRWM
US Department of Energy
1000 Independence Avenue SW
Washington, DC 20585

1 R. M. Nelson (RW-20)
Office of Geologic Disposal
OCRWM
US Department of Energy
1000 Independence Avenue SW
Washington, DC 20585

1 S. J. Brocoum (RW-22)
Analysis and Verification Division
OCRWM
US Department of Energy
1000 Independence Avenue SW
Washington, DC 20585

1 D. Shelor (RW-30)
Office of Systems and Compliance
OCRWM
US Department of Energy
1000 Independence Avenue SW
Washington, DC 20585

1 J. Roberts (RW-33)
Director, Regulatory Compliance
Division
OCRWM
US Department of Energy
1000 Independence Avenue SW
Washington, DC 20585

1 G. J. Parker (RW-332)
Reg. Policy/Requirements Branch
OCRWM
US Department of Energy
1000 Independence Avenue SW
Washington, DC 20585

1 R. A. Milner (RW-40)
Office of Storage and
Transportation
OCRWM
US Department of Energy
1000 Independence Avenue SW
Washington, DC 20585

1 D. R. Elle, Director
Environmental Protection Division
DOE Nevada Field Office
US Department of Energy
P.O. Box 98518
Las Vegas, NV 89193-8518

1 T. Wood (RW-52)
Director, M&O Management Division
OCRWM
US Department of Energy
1000 Independence Avenue SW
Washington, DC 20585

4 Victoria F. Reich, Librarian
Nuclear Waste Technical Review Board
1100 Wilson Blvd., Suite 910
Arlington, VA 22209

5 Wesley Barnes, Project Manager
Yucca Mountain Site
Characterization Office
US Department of Energy
P.O. Box 98608–MS 523
Las Vegas, NV 89193-8608

1 C. L. West, Director
Office of External Affairs
DOE Nevada Field Office
US Department of Energy
P.O. Box 98518
Las Vegas, NV 89193-8518

8 Technical Information Officer
DOE Nevada Field Office
US Department of Energy
P.O. Box 98518
Las Vegas, NV 89193-8518

1 P. K. Fitzsimmons, Technical Advisor
Office of Assistant Manager for
Environmental Safety and Health
DOE Nevada Field Office
US Department of Energy
P.O. Box 98518
Las Vegas, NV 89193-8518

1 J. A. Blink
Deputy Project Leader
Lawrence Livermore National Lab.
101 Convention Center Drive
Suite 820, MS 527
Las Vegas, NV 89109

4 J. A. Canepa
Technical Project Officer - YMP
N-5, Mail Stop J521
Los Alamos National Laboratory
P.O. Box 1663
Los Alamos, NM 87545

1 H. N. Kalia
Exploratory Shaft Test Manager
Los Alamos National Laboratory
Mail Stop 527
101 Convention Center Dr., #820
Las Vegas, NV 89109

1 Repository Licensing & Quality Assurance
Project Directorate
Division of Waste Management
US NRC
Washington, DC 20555

1 Senior Project Manager for Yucca Mountain
Repository Project Branch
Division of Waste Management
US NRC
Washington, DC 20555

1 NRC Document Control Desk
Division of Waste Management
US NRC
Washington, DC 20555

1 Chad Glenn
NRC Site Representative
301 E Stewart Avenue, Room 203
Las Vegas, NV 89101

1 E. P. Binnall
Field Systems Group Leader
Building 50B/4235
Lawrence Berkeley Laboratory
Berkeley, CA 94720

1 Center for Nuclear Waste
Regulatory Analyses
6220 Culebra Road
Drawer 28510
San Antonio, TX 78284

3 W. L. Clarke
Technical Project Officer - YMP
Attn: YMP/LRC
Lawrence Livermore National
Laboratory
P.O. Box 5514
Livermore, CA 94551

1 V. R. Schneider
Asst. Chief Hydrologist–MS 414
Office of Program Coordination
and Technical Support
US Geological Survey
12201 Sunrise Valley Drive
Reston, VA 22092

1 J. S. Stuckless
Geologic Division Coordinator
MS 913
Yucca Mountain Project
US Geological Survey
P.O. Box 25046
Denver, CO 80225

1 N. Z. Elkins
Deputy Technical Project Officer
Los Alamos National Laboratory
Mail Stop 527
101 Convention Center Drive, #820
Las Vegas, NV 89109

5 L. S. Costin, Acting
Technical Project Officer - YMP
Sandia National Laboratories
Organization 6313, MS 1325
P.O. Box 5800
Albuquerque, NM 87185

1 J. F. Devine
Asst Director of Engineering Geology
US Geological Survey
106 National Center
12201 Sunrise Valley Drive
Reston, VA 22092

1 L. R. Hayes
Technical Project Officer
Yucca Mountain Project Branch
MS 425
US Geological Survey
P.O. Box 25046
Denver, CO 80225

1 A. L. Flint
US Geological Survey
MS 721
P.O. Box 327
Mercury, NV 89023

1 D. A Beck
Water Resources Division, USGS
6770 S. Paradise Road
Las Vegas, NV 89119

1 P. A. Glancy
US Geological Survey
Federal Building, Room 224
Carson City, NV 89701

1 Sherman S. C. Wu
US Geological Survey
2255 N. Gemini Drive
Flagstaff, AZ 86001

1 J. H. Sass - USGS
Branch of Tectonophysics
2255 N. Gemini Drive
Flagstaff, AZ 86001

1 D. H. Appel, Chief
Hydrologic Investigations Program
MS 421
US Geological Survey
P.O. Box 25046
Denver, CO 80225

1 E. J. Helley
Branch of Western Regional Geology
MS 427
US Geological Survey
345 Middlefield Road
Menlo Park, CA 94025

1 R. W. Craig, Chief
Nevada Operations Office
US Geological Survey
101 Convention Center Drive
Suite 860, MS 509
Las Vegas, NV 89109

1 D. Zesiger
US Geological Survey
101 Convention Center Drive
Suite 860, MS 509
Las Vegas, NV 89109

1 G. L. Ducret, Associate Chief
Yucca Mountain Project Division
US Geological Survey
P.O. Box 25046
421 Federal Center
Denver, CO 80225

2 L. D. Foust
Nevada Site Manager
TRW Environmental Safety Systems
101 Convention Center Drive
Suite 540, MS 423
Las Vegas, NV 89109

1 C. E. Ezra
YMP Support Office Manager
EG&G Energy Measurements Inc.
MS V-02
P.O. Box 1912
Las Vegas, NV 89125

1 Jan Docka
Roy F. Weston, Inc.
955 L'Enfant Plaza SW
Washington, DC 20024

1 Technical Information Center
Roy F. Weston, Inc.
955 L'Enfant Plaza SW
Washington, DC 20024

1 DeWayne Campbell
Technical Project Officer - YMP
US Bureau of Reclamation
Code D-3790
P.O. Box 25007
Denver, CO 80225

1 J. M. LaMonaca
Records Specialist
US Geological Survey
421 Federal Center
P.O. Box 25046
Denver, CO 80225

1 W. R. Keefer - USGS
913 Federal Center
P.O. Box 25046
Denver, CO 80225

1 M. D. Voegele
Technical Project Officer - YMP
SAIC
101 Convention Center Drive
Suite 407
Las Vegas, NV 89109

1 Paul Eslinger, Manager
PASS Program
Pacific Northwest Laboratories
P.O. Box 999
Richland, WA 99352

1 A. T. Tamura
Science and Technology Division
OSTI
US Department of Energy
P.O. Box 62
Oak Ridge, TN 37831

1 Carlos G. Bell, Jr.
Professor of Civil Engineering
Civil and Mechanical Engineering Dept.
University of Nevada, Las Vegas
4505 S. Maryland Parkway
Las Vegas, NV 89154

1 P. J. Weeden, Acting Director
Nuclear Radiation Assessment Div.
US EPA
Environmental Monitoring Sys. Lab
P.O. Box 93478
Las Vegas, NV 89193-3478

1 ONWI Library
Battelle Columbus Laboratory
Office of Nuclear Waste Isolation
505 King Avenue
Columbus, OH 43201

1 D. Hedges, Vice President, QA
Roy F. Weston, Inc.
4425 Spring Mountain Road
Suite 300
Las Vegas, NV 89102

1 D. L. Fraser, General Manager
Reynolds Electrical & Engineering
Company, Inc.
MS 555
P.O. Box 98521
Las Vegas, NV 89193-8521

1 B. W. Colston, President & Gen. Mgr.
Las Vegas Branch
Raytheon Services Nevada
MS 416
P.O. Box 95487
Las Vegas, NV 89193-5487

1 R. L. Bullock
Technical Project Officer - YMP
Raytheon Services Nevada
Suite P-250, MS 403
101 Convention Center Drive
Las Vegas, NV 89109

1 C. H. Johnson
Technical Program Manager
Agency for Nuclear Projects
State of Nevada
Evergreen Center, Suite 252
1802 N. Carson Street
Carson City, NV 89710

1 John Fordham
Water Resources Center
Desert Research Institute
P.O. Box 60220
Reno, NV 89506

1 David Rhode
Desert Research Institute
P.O. Box 60220
Reno, NV 89506

1 Eric Anderson
Mountain West Research Southwest Inc.
2901 N. Central Avenue, #1000
Phoenix, AZ 85012-2730

1 The Honorable Cyril Schank
Chairman
Churchill County Board of
Commissioners
190 W. First Street
Fallon, NV 89406

1 T. Hay, Executive Assistant
Office of the Governor
State of Nevada
Capitol Complex
Carson City, NV 89710

3 R. R. Loux
Executive Director
Agency for Nuclear Projects
State of Nevada
Evergreen Center, Suite 252
1802 N. Carson Street
Carson City, NV 89710

1 Brad Mettam
Inyo County Yucca Mountain
Repository Assessment Office
Drawer L
Independence, CA 93526

1 Lander County Board of
Commissioners
315 South Humbolt
Battle Mountain, NV 89820

1 Vernon E. Poe
Office of Nuclear Projects
Mineral County
P.O. Box 1026
Hawthorne, NV 89415

1 Les W. Bradshaw
Program Manager
Nye County Repository
P.O. Box 429
Tonopah, NV 89049

1 Florindo Mariani
White Pine County Nuclear
Waste Project Office
457 Fifth Street
Ely, NV 89301

1 Judy Foremaster
City of Caliente Nuclear Waste
Project Office
P.O. Box 158
Caliente, NV 89008

1 Philip A. Niedzielski-Eichner
Nye County Nuclear Waste
Repository Project Office
P.O. Box 221274
Chantilly, VA 22022-1274

1 Dennis Bechtel, Coordinator
Nuclear Waste Division
Clark County Department of
Comprehensive Planning
301 E. Clark Avenue, Suite 570
Las Vegas, NV 89101

1 Juanita D. Hoffman
Nuclear Waste Repository
Oversight Program
Esmeralda County
P.O. Box 490
Goldfield, NV 89013

1 Eureka County Board of Commissioners
Yucca Mountain Information Office
P.O. Box 714
Eureka, NV 89316

1 Economic Development Dept.
City of Las Vegas
400 E. Stewart Avenue
Las Vegas, NV 89101

1 Community Planning & Development
City of North Las Vegas
P.O. Box 4086
North Las Vegas, NV 89030

1 Community Development & Planning
City of Boulder City
P.O. Box 61350
Boulder City, NV 89006

1 Commission of European Communities
200 Rue de la Loi
B-1049 Brussells
BELGIUM

2 M. J. Dorsey, Librarian
YMP Research & Study Center
Reynolds Electrical & Engineering
Company, Inc.
MS 407
P.O. Box 98521
Las Vegas, NV 89193-8521

1 Amy Anderson
Argonne National Laboratory
Building 362
9700 S. Cass Avenue
Argonne, IL 60439

1 Steve Bradhurst
P.O. Box 1510
Reno, NV 89505

1 Michael L. Baughman
35 Clark Road
Fiskdale, MA 01518

1 Glenn Van Roekel
Director of Community Development
City of Caliente
P.O. Box 158
Caliente, NV 89008

1 Jason Pitts
Lincoln County Nuclear Waste
Project Office
Lincoln County Courthouse
Pioche, NV 89043

1 Ray Williams, Jr.
P.O. Box 10
Austin, NV 89310

1 Nye County District Attorney
P.O. Box 593
Tonopah, NV 89049

1 William Offutt
Nye County Manager
Tonopah, NV 89049

1 Charles Thistlethwaite, AICP
Associate Planner
Inyo County Planning Department
Drawer L
Independence, CA 93526

1 R. F. Pritchett
Technical Project Officer - YMP
Reynolds Electrical & Engineering
Company, Inc.
MS 408
P.O. Box 98521
Las Vegas, NV 89193-8521

1 Dr. Moses Karakouzian
1751 E. Reno, #125
Las Vegas, NV 89119

10 Dr. R. J. Martin III
76 Olcott Drive
White River Junction, VT 05001

	MS	
20	1325	R. H. Price, 6313
2	1330	C. B. Michaels, 6352 100/1232713/SAND94-2585/QA
20	1330	WMT Library, 6352
1	9018	Central Technical Files, 8523-2
5	0899	Technical Library, 13414
1	0619	Print Media, 12615
2	0100	Document Processing, 7613-2 for DOE/OSTI